Journal of Catalysis 377 (2019) 692–710

Contents lists available at ScienceDirect

Journal of Catalysis

journal homepage: www.elsevier.com/locate/jcat

Reactivity and selectivity descriptors of dioxygen activation routes on metal oxides

Stephanie Kwon [a], Prashant Deshlahra [b], Enrique Iglesia [a,*]

[a] *Department of Chemical Engineering, University of California at Berkeley, Berkeley, CA 94720, United States*
[b] *Department of Chemical and Biological Engineering, Tufts University, Medford, MA 02155, United States*

ARTICLE INFO

Article history:
Received 27 March 2019
Revised 22 July 2019
Accepted 23 July 2019

Keywords:
Oxidation catalysis
Redox cycle
Dioxygen activation
Density functional theory
Metal oxides

ABSTRACT

The activation of dioxygen at typically isolated two-electron reduced centers can lead to the formation of electrophilic superoxo or peroxo species, providing an essential route to form reactive O_2-derived species in biological, organometallic, and heterogeneous catalysts. Alternatively, O_2 activation can proceed via outer sphere routes, circumventing the formation of bound peroxo (OO*) species during oxidation catalysis by forming H_2O_2(g), which can react with another reduced center to form H_2O. The electronic and binding properties of metal oxides that determine the relative rates of these activation routes are assessed here by systematic theoretical treatments using density functional theory (DFT). These methods are combined with conceptual frameworks based on thermochemical cycles and crossing potential models to assess the most appropriate descriptors for the activation barriers for each route using Keggin polyoxometalates as illustrative examples. In doing so, we show that inner sphere routes, which form OO* species via O_2 activation on the O-vacancies (*) formed in the reduction part of redox cycles, are mediated by early transition states that only weakly sense the oxide binding properties. Outer sphere routes form H_2O_2(g) via O_2 activation on OH pairs (H/OH*) formed by dissociation of H_2O on O-vacancies; their rates and activation barriers reflect the rates of the first H-atom transfer from H/OH* to O_2. The activation barriers for this H-transfer step depend on the binding energy of more weakly-bound H-atom in H/OH* pairs (HAE_2) and on the ·OOH-surface interaction energy at its product state (E_{int}^{0}). The E_{int}^{0} values are similar among oxides unless a large charge-balancing cation is present and interacts with ·OOH; consequently, HAE_2 acts as an appropriate descriptor of the outer sphere dynamics. HAE_2 also determines the thermodynamics of H_2O dissociation on O-vacancies, which influence the inner and outer sphere rates by setting the relative coverage of * and H/OH*. These results, in turn, show that HAE_2 is a complete descriptor of the reactivity and selectivity of oxides for O_2 activation; the O-atoms in more reducible oxides (more negative HAE_2) exhibit a greater preference for the inner sphere routes and for the formation of electrophilic OO* intermediates that mediate epoxidation and O-insertion reactions during catalytic redox cycles. Large charge-balancing cations locally modify E_{int}^{0} values that determine the outer sphere rates and thus can be used to alter the preference of O-atoms to either inner or outer sphere routes.

© 2019 Elsevier Inc. All rights reserved.

1. Introduction

O_2 activation steps are essential to complete Mars-van Krevelen redox cycles that mediate catalytic oxidation turnovers on reducible metal oxides [1–3]. In oxidative dehydrogenation (ODH) reactions, the abstraction of two H-atoms from organic substrates by vicinal lattice O-atoms (O*) adds two protons on the surface O-atoms and two electrons in the lowest unoccupied molecular orbital (LUMO) of the oxides. These two-electron reduced centers, which can be present in the form of vicinal hydroxyls (H/OH*) or O-vacancies (*) upon the re-combinative desorption of H_2O, must be re-oxidized through reactions with O_2 in order to restore the nucleophilic lattice O-atoms (O*) required for subsequent ODH turnovers [4,5]. Such re-oxidation events can involve electrophilic O_2-derived intermediates (e.g., superoxide, peroxide) formed by reactions of O_2 on O-vacancies (*) (step 1; Scheme 1) [5,6]; these pathways have been denoted as "inner sphere" routes because they restore the M-O bonds removed during the reduction part of redox cycles [7–9]. Alternate "outer sphere" routes, in contrast, involve the activation of O_2 on H/OH* to form H_2O_2(g) and the O-atom pairs (step 3; Scheme 1) without the cleavage or reformation of M-O bonds as part of the O_2 activation process [4,8]. The two types of reduced centers (* and H/OH*) involved in these

---

* Corresponding author.
E-mail address: iglesia@berkeley.edu (E. Iglesia).

https://doi.org/10.1016/j.jcat.2019.07.048
0021-9517/© 2019 Elsevier Inc. All rights reserved.

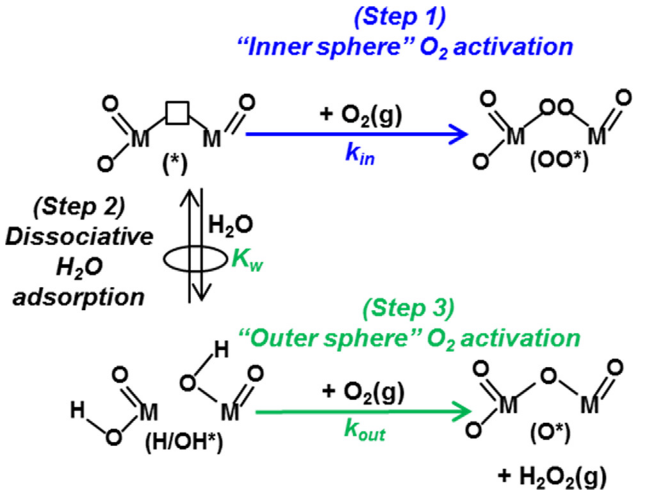

Scheme 1. Elementary steps involved in O_2 activation on two-electron reduced centers in the forms of O-vacancies (*) and vicinal hydroxyl pairs (H/OH*) via inner and outer sphere routes. A quasi-equilibrated step is denoted by an oval symbol placed over double arrows. Nomenclature used here to denote each reactive species is shown in parentheses under each structure.

two O_2 activation routes are present at relative coverages dictated by the equilibrium of dissociative H_2O adsorption on * during steady-state catalytic oxidation reactions (step 2; Scheme 1).

The relative contributions of inner and outer sphere routes to re-oxidation rates influence the reactivity and selectivity of oxide surfaces by determining the prevalent O_2-derived intermediates (OO* and H_2O_2(g)) involved. H_2O_2(g) species formed via outer sphere routes (step 3; Scheme 1) can react with non-vicinal reduced centers (* or H/OH*), thus acting as a molecular shuttle that becomes essential when reduced centers are located at distances beyond molecular dimensions, as is the case at low concentrations of reduced centers prevalent during oxidation catalysis. The bound OO* species involved in the inner sphere routes (step 1; Scheme 1), in contrast, react with gaseous molecules (reactants, primary products, or added scavenging molecules) via O-insertion elementary steps in order to complete four-electron oxidation events by O_2 and to regenerate the O* centers required for subsequent catalytic turnovers. Such OO* reaction pathways, proposed previously from kinetic scavenging and theoretical methods, circumvent the large kinetic barriers for OO* migration, which would be otherwise required for the re-oxidation of two non-vicinal reduced centers by O_2 [4]. These O-insertion elementary steps mediated by OO* intermediates, however, can lead to unselective oxidations with O_2 by converting primary products to undesired CO_x products [5].

Oxide systems that circumvent the formation of OO* intermediates during the re-oxidation part of the cycle may prevent O-insertion reactions that can form CO_x products (CO, CO_2) in ODH reactions [4,5]. Such OO* species, however, mediate epoxidation routes that are often intended and desired in practice [6]. Methane monooxygenase enzymes are also thought to use OO* species formed during O_2 activation on two-electron reduced centers to mediate O-insertion into a strong C-H bond in CH_4 to form CH_3OH [10]. Many efforts to mimic monooxygenase pathways on inorganic oxides, however, have failed to achieve significant CH_3OH yields [11–14], because of kinetic hurdles and side reactions that remain the subject of active inquiry. In spite of the significant impact of O_2 activation routes in the practice of oxidation catalysis, the specific binding properties of oxide surfaces that determine the relative contributions of inner and outer sphere routes have remained unclear; they have not been addressed by systematic experimental and theoretical studies of O_2 activation dynamics during catalytic oxidation cycles on redox-active solids with diverse compositions and structures.

Mechanistic inquiries into O_2 activation routes are seldom accessible by direct observation, because their dynamics are kinetically-inconsequential for turnover rates in most oxidation reactions (ODH of alkanes [15–19] and alkanols [20,21]). Less direct methods available include theoretical treatments of the energies of plausible intermediates and transition states involved in re-oxidation events [4], the scavenging of bound peroxo-type intermediates with organic substrates to form detectable epoxidation products [4], and transient spectroscopic measurements that independently probe reduction and oxidation rate constants [22]. Theoretical methods can also be used to probe the specific binding properties of redox-active oxides that determine the rates and selectivities of inner and outer sphere O_2 activation routes through a rigorous assessment of O_2 activation dynamics and thermodynamics on realistic oxide surfaces.

Reactions of O_2 with two-electron reduced centers involve complex triplet-singlet spin crossings and radical-like intermediates along their reaction coordinate; these spin states must be rigorously captured by theoretical methods in order to obtain accurate energies and to reach correct conclusions. These calculations also require realistic structural models of oxides that accurately capture the chemical and geometric features of catalytically-relevant redox-active oxides. In these contexts, Keggin-type polyoxometalate (POM) clusters are ideally suited as illustrative oxides; their known structures and compositional diversity allow direct comparisons with experiment, as well as access to lattice O-atoms with octahedral coordination environments and a broad range of binding properties [23–25]. POM clusters have been previously used to benchmark scavenging experiments during alkanol ODH and DFT-derived estimates of inner and outer sphere O_2 activation barriers [4] and to determine the most appropriate catalyst and molecular descriptors of rates and selectivities for the activation of strong C-H bonds in organic molecules by nucleophilic lattice O-atoms at the surfaces of redox-active oxides [26].

Here, density functional theory (DFT) methods are used to determine the energies of intermediates and transition states that mediate inner and outer sphere O_2 activation routes. These energies are determined for lattice O-atoms present at different locations in POM clusters with diverse compositions, which form and use reduced centers as part of catalytic redox cycles. The trends observed are used to construct a conceptual and practical framework that combines: (i) crossing-potential models to assess the lateness of transition states; (ii) thermochemical cycles that dissect reaction energies into the relevant properties of the solid oxides and of the molecules; and (iii) H-addition tendencies of lattice O-atoms in oxides as accurate descriptors of O_2 activation rates and selectivities. Such a formalism allows accurate theoretical inquiries into the oxide structures and compositions that select inner or outer sphere routes for dioxygen activation, providing design strategies for solid oxides that favor nucleophilic or electrophilic attack on organic substrates.

2. Computational methods

Plane-wave DFT methods were implemented using the Vienna *ab initio* simulation package (VASP) [27–29]. Electronic energies were determined using the generalized gradient approximation (GGA) method with the Perdew-Wang exchange-correlation functional (PW91) [30]. The plane-wave basis-set was expanded up to an energy cutoff of 400 eV and the core-valence interactions of electrons were treated using projector-augmented wave (PAW) methods [31,32]. Energies were optimized until the energy difference between successive iterations was less than 1×10^{-6} eV and the atomic locations were relaxed until the forces on each atom were less than 0.05 eV $Å^{-1}$. The first Brillouin zone was sampled using a 1 × 1 × 1 Monkhorst-Pack [33] k-point grid.

The structures and energies of POM clusters, intermediates, transition states, and products for O_2 activation routes, and of all gaseous molecules were calculated by placing them at the center of a 2 × 2 × 2 nm box in order to minimize interactions among periodic images in adjacent unit cells by an intervening vacuum gap; a larger box (3 × 3 × 3 nm) gave the similar energies for intermediates and transition states [4]. All atoms were fully relaxed except the central atom, which was fixed to prevent the shifting of POM clusters during each energy iteration. The placement of a single reduced center and an O_2-derived intermediate on the POM clusters breaks the symmetry of each cell, inducing dipole moments that can result in significant errors for periodic systems; these artifacts were corrected by calculating dipole and quadrupole moments at the center of the unit cell and subtracting interaction energies among these moments from DFT-derived energies that contain such interactions in addition to electronic energies of isolated systems [34].

POM clusters with different addenda atoms (Mo, Mo-V, W), central atoms (Al^{3+}, P^{5+}), and charge-balancing cations (H^+, NH_4^+) were used to probe the energies of intermediates and transition states involved in inner and outer sphere O_2 activation routes; their crystallographic structures are shown in Fig. 1. The O-atoms at O_1 location in Fig. 1 were removed from these clusters to form O-vacancies; these O-atoms were chosen because they are among the most reactive O-atoms for H-abstraction from organic molecules and, as a result, they represent the predominant locations of reduced centers as they form during catalytic redox cycles. These conclusions and calculation strategies are supported by DFT-derived H-atom addition energies (HAE) at each O-atom location and they represent an accurate descriptor of C-H activation reactivity on redox-active oxides [4,35]. One, two, or three charge-balancing protons in $H_3PMo_{12}O_4$ were replaced with NH_4^+ to assess the influence of charge-balancing cations on the O_2 activation dynamics and thermodynamics; for $(NH_4)_2H_1PMo_{12}O_{40}$ clusters, two protons that are either vicinal or distant to the O_1 location are substituted with NH_4^+ (denoted as $(NH_4)_2H_1PMo_{12}O_{40}$ (a) and (b) in Fig. 1, respectively) in order to verify any interaction between NH_4^+ and the O_2 activation intermediates and transition states. The O-vacancies formed at different O-atom locations were also considered in the case of $H_3PMo_{12}O_{40}$, $H_3PW_{12}O_{40}$ and $H_5PV_2Mo_{10}O_{40}$ clusters in order to assess any effects of location on the energies of intermediates and transition states along the O_2 activation reaction coordinates. In the case of $H_5PV_2Mo_{10}O_{40}$, these O-atoms include the one that bridges the Mo and V atoms (Mo-O-V; O_1 location in $H_5PV_2Mo_{10}O_{40}$; Fig. 1) and the other that connects two Mo atoms at a location distant from the V-atom (O_3 location in $H_5PV_2Mo_{10}O_{40}$; Fig. 1); for $H_3PMo_{12}O_{40}$ and $H_3PW_{12}O_{40}$ clusters, O-atom locations were chosen to sample sites with significantly different HAE values in the same cluster and differing in their distance from the O_1 location.

Electronic energies of POM clusters, intermediates, and products for O_2 activation routes are calculated in their singlet states (spin-restricted and spin-polarized) as well as in triplet states in order to verify their lowest energy spin configurations. All POM clusters examined here are more stable in their spin-restricted singlet state (no unpaired electron) than in their triplet state (two electrons with unpaired spins); their energies in spin-restricted and spin-polarized singlet states differ by < 1 kJ mol^{-1}, confirming that all electrons are paired in POM clusters. The spin-restricted singlet state remains the most stable configuration for POM clusters after the removal of an O-atom to form an O-vacancy (*) and after the addition of two H-atoms to an O-atom pair to form vicinal OH pair (H/OH*). Gaseous O_2 molecules, in contrast, are more stable in the triplet state (two unpaired electrons in the p-orbital of each O-atom) and a weakly-bound O_2 on * or H/OH* center remains more stable in its triplet state than in its singlet state. The activation of such weakly-bound O_2 species requires a two-electron transfer from a POM cluster containing a two-electron reduced center (* or H/OH*) to form OO* or H_2O_2(g) product via inner or outer sphere routes (steps 1 and 3 in Scheme 1). This two-electron transfer process leads to the pairing of electrons in O_2-moieties and to spin-restricted singlet state as the most stable configuration in the product states of O_2 activation. The spin changes along the reaction coordinate, in turn, require that triplet (reactant) and singlet (product) potential energy surfaces (PES) cross along the O_2 activation reaction coordinate. Such a phenomenon involving two states of spin multiplicities along the minimum-energy pathway is known as two-state reactivity [36,37]; in such cases, the energy consequences of spin-orbit coupling that can lead to the stabilization of the intermediates and transition states located at the spin-crossing points [26,38] become critical. These triplet-singlet spin-crossings are described here by calculating (spin-polarized) singlet and triplet PES that connect reactants and products in (spin-polarized) singlet and triplet states, respectively, using nudge elastic band (NEB) methods [39]; these two PES are combined to derive minimum energy paths (MEP) by comparing and selecting the lowest energy state of reactants and intermediates along the O_2 activation reaction coordinate. The spin-coupling effects on the energies of intermediates and transition states at the spin-crossing points are assessed by comparing their energies in a broken-symmetry configuration (spin-polarized singlet) to those in spin-restricted singlet and triplet states and selecting the lowest energy. Henkelman's Dimer method [40] was used to derive the transition state structures using the NEB images at the highest point along the minimum energy pathways (MEP) and at the triplet-singlet crossing points as initial guesses.

Accurate estimations of rates and rate ratios require free energies (G) that include their enthalpy (H) and entropy (S) components at the reaction temperatures of interest. Enthalpies include DFT-derived electronic energies (E_0) at 0 K, zero-point vibrational energies (ZPVE), and the contributions from vibrations and from translations and rotations for gaseous species (H_2O and O_2) at finite temperatures:

$$H = E_0 + ZPVE + H_{vib} + H_{trans} + H_{rot} \tag{1}$$

The entropies (S) are given by:

$$S = S_0 + \ S_{vib} + S_{trans} + S_{rot} \tag{2}$$

ZPVE and vibrational, rotational, and translational contributions in enthalpies and entropies were derived from statistical mechanical formalisms [41]. Vibrational frequencies were calculated for DFT-derived structures using VASP by diagonalizing the Hessian matrices derived from energy changes upon perturbation of each atom in the O_2-moeities and the POM cluster in x, y and z directions (by ±0.001 nm). Low frequency vibrational modes (<100 cm^{-1}) of weakly-bound O_2-derived species tend to give inaccurate entropy values; these modes represent frustrated translational and rotational modes of the gas-phase O_2 molecule. The contributions of these low modes to the entropies and enthalpies are thus instead calculated by replacing them with a fraction (0.7) of the translational and rotational modes of gaseous O_2. Such a treatment is inspired by a previous experimental study on well-defined oxide surfaces, which has shown that the weakly-bound molecules on such surfaces tend to retain approximately 0.7 fraction of their gas-phase entropies [42]. The details of such thermodynamic treatments of low frequency modes were shown in previous studies [21,26].

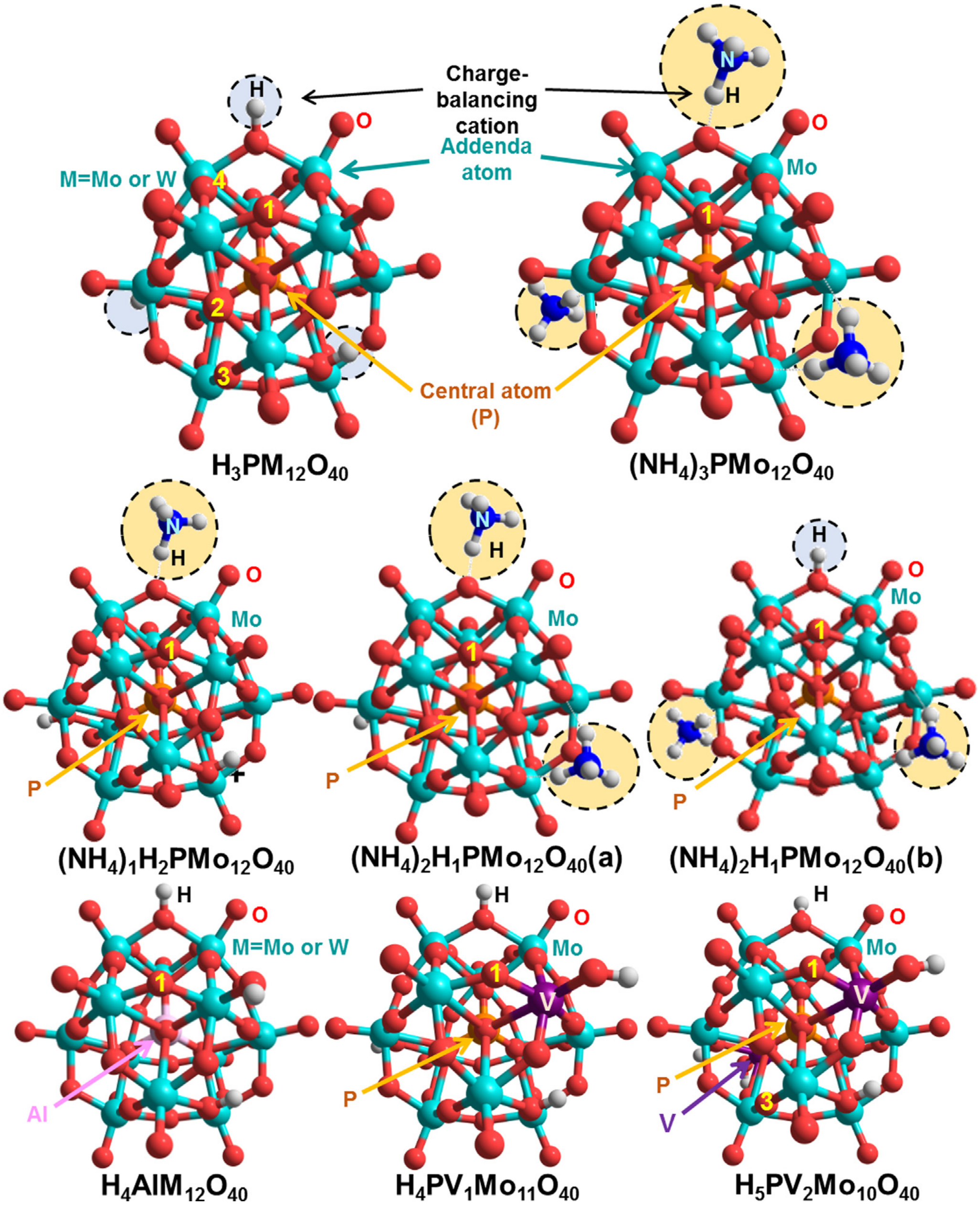

Fig. 1. DFT-derived structures of Keggin POM clusters: $H_3PM_{12}O_{40}$ (M = Mo or W), $(NH_4)_nH_{3\text{-}n}PMo_{12}O_{40}$ (n = 1–3), $H_4AlM_{12}O_{40}$ (M = Mo or W), $H_4PV_1Mo_{11}O_{40}$, and $H_5PV_2Mo_{10}O_{40}$. The specific locations of O-atoms that are removed to form O-vacancies in probing energies of intermediates and transition states involved in O_2 activation routes are numbered in each POM cluster. The charge-balancing cations (H^+ and NH_4^+) in $H_3PM_{12}O_{40}$ and $(NH_4)_nH_{3\text{-}n}PMo_{12}O_{40}$ (n = 1–3) clusters are highlighted using dashed circles.

The results reported here are from DFT calculations using PW91 functionals without the inclusion of Hubbard U interactions [43,44] because PW91+U methods tend to overestimate the reducibility of the POM clusters and give the C-H bond activation barriers (for the reduction part of the cycle) that are much lower than those determined from experiments [21]. The use of PW91+U method (with $U_{eff} = 8.6$, the value suggested previously for Mo [45]) also leads to the prediction that O_2 activation routes are endothermic (Table S.1; Supporting Information, Section S.1). Such a prediction contradicts kinetic observations during CH_3OH ODH on the same $H_3PMo_{12}O_{40}$ cluster [4,35], which show that reoxidation of reduced centers is very fast and thus they present as trace species during catalysis, the essential requirement for sole kinetic relevance of the C-H activation step and the kinetically-irrelevance of O_2 activation steps.

The effects of computational methods on H-atom addition energy (HAE), the errors in gas-phase energies of O_2 and H_2O_2 molecules, and the trend in O_2 activation barriers are discussed in the Supporting Information (Section S.1, Tables S.2-S.4, and Fig. S.1) by comparing the values shown in this work (VASP/PW91/PAW) to those derived using hybrid-DFT methods (HSE06 and B3LYP) with plane-wave-basis sets (as implemented in the VASP software) and with localized atomic basis sets (in the Gaussian program). These results, in turn, show that (i) HAE values derived from periodic hybrid-DFT methods (HSE06 and B3LYP/VASP/PAW) are similar (−317 vs. −321 kJ mol^{-1}) and only slightly more negative than those derived with PW91 functionals (−295 kJ mol^{-1}) and (ii) both DFT (PW91) and hybrid-DFT (HSE06 and B3LYP) methods lead to considerable errors in energies of O_2(g) (+19 to +57 kJ mol^{-1}; Table S.3) and H_2O_2(g) (−17 to

−11 kJ mol^{-1}; Table S.4), which depend sensitively on the choice of functionals and basis-sets. Such errors in O_2 energies, however, tend to cancel out in calculating activation barriers because transition states mediating inner and outer sphere routes involve O=O bonds that are nearly unperturbed from gas-phase O_2. As a result, the outer sphere O_2 activation barriers derived using GGA (PW91) and hybrid (B3LYP) functionals lie on the same trend line when plotted as a function of the summated energies of the negative value of HAE_2 and ·OOH-surface interaction energies at the product states ($E_{int}{}^0$-HAE_2; the catalytic descriptor of the outer sphere O_2 activation routes, Section 3.2) (Fig. S.1).

3. Results and discussion

Redox-active oxides form and use two-electron reduced centers that can take the form of O-vacancies (*; Scheme 1) or vicinal hydroxyl pairs (H/OH*; Scheme 1); these species act as intermediates in Mars-van Krevelen catalytic cycles [1,35]. These two types of reduced centers (* and H/OH*) lead to the formation of OO* and H_2O_2(g) products, respectively, via inner and outer O_2 activation routes (steps 1 and 3; Scheme 1). Their rate ratios (r_{in}/r_{out}, defined as χ) are given by [4]:

$$\frac{r_{in}}{r_{out}} = \frac{k_{in}P_{O_2}[*]}{k_{out}P_{O_2}[H/OH*]} = \frac{k_{in}}{k_{out}K_wP_{H_2O}} = \chi, \tag{3}$$

where [*] and [H/OH*] are the surface coverages of O-vacancies and vicinal hydroxyl pairs. The first-order rate constants for inner and outer sphere O_2 activation routes (k_{in} and k_{out} for steps 1 and 3; Scheme 1) reflect the free energy differences between their transition states ($G_{in}{}^{TS}$ and $G_{out}{}^{TS}$) and the respective bound precursors (* and H/OH*) and one O_2(g):

$$k_{in} = \frac{k_BT}{h}exp\left(-\left(\frac{G_{in}{}^{TS} - G_* - G_{O_2}}{RT}\right)\right) = \frac{k_BT}{h}exp\left(-\left(\frac{\Delta G_{in}{}^{TS}}{RT}\right)\right) \tag{4}$$

$$\begin{aligned} k_{out} &= \frac{k_BT}{h}exp\left(-\left(\frac{G_{out}{}^{TS} - G_{H/OH*} - G_{O_2}}{RT}\right)\right) \\ &= \frac{k_BT}{h}exp\left(-\left(\frac{\Delta G_{out}{}^{TS}}{RT}\right)\right) \end{aligned} \tag{5}$$

Here, T is temperature, k_B is the Boltzmann's constant, h is the Planck's constant, and R is the gas constant. K_w in Eq. (3) is the equilibrium constant for H_2O dissociation on * to form H/OH* (step 2; Scheme 1). Its magnitude reflects the free energy differences between H/OH* species and their * and H_2O(g) precursors (ΔG_{H_2O}) :

$$K_w = exp\left(-\left(\frac{G_{H/OH*} - G_* - G_{H_2O}}{RT}\right)\right) = exp\left(\left(\frac{\Delta G_{H_2O}}{RT}\right)\right) \tag{6}$$

Eqs. (3)–(6), taken together, give the ratio of inner and outer sphere rates (χ) as a function of the free energies of inner and outer sphere transition states ($G_{in}{}^{TS}$ and $G_{out}{}^{TS}$), which depend on the oxide structure and composition, and of the free energy of H_2O(g) (G_{H_2O}):

$$\begin{aligned} \chi &= exp\left[\frac{-\left(\Delta G_{in}{}^{TS} - (\Delta G_{out}{}^{TS} + \Delta G_{H_2O})\right)}{RT}\right]\frac{1}{P_{H_2O}} \\ &= exp\left[\frac{-\left(G_{in}{}^{TS} + G_{H_2O} - G_{out}{}^{TS}\right)}{RT}\right]\frac{1}{P_{H_2O}} \end{aligned} \tag{7}$$

DFT methods are used here to calculate the electronic energies of inner and outer sphere transition states ($E_{in}{}^{TS}$ and $E_{out}{}^{TS}$) for the reduced centers (* and H/OH*) formed at different O-atom locations in the POM clusters with diverse chemical compositions; the range of O-atom locations and POM compositions examined in this work is shown in Fig. 1. These energies are then used to derive the corresponding free energies at relevant conditions (chosen here as 453 K; 1 bar O_2) via Eqs. (1) and (2) using the statistical mechanical treatments described above; these free energies are used to assess the relative rates of inner and outer sphere routes via Eq. (7). The combined magnitude of the free energy difference between inner and outer sphere transition states and the free energy of H_2O molecules ($G_{in}{}^{TS} + G_{H_2O} - G_{out}{}^{TS}$) determines the rate ratio (r_{in}/r_{out}, χ; Eq. (7)). These ($G_{in}{}^{TS} + G_{H_2O} - G_{out}{}^{TS}$) values scale linearly with the corresponding electronic energy components ($E_{in}{}^{TS} + E_{H_2O} - E_{out}{}^{TS}$) with a slope near unity (0.98 ± 0.07; Fig. S.2; Supporting Information), indicating that the differences of ZPVE and thermal contributions to enthalpies and entropies between inner and outer sphere routes are similar among O-atom locations and POM compositions. The specific binding properties of lattice O-atoms in oxides that influence the inner and outer TS electronic energies ($E_{in}{}^{TS}$ and $E_{out}{}^{TS}$) are examined next using a formalism that exploits crossing-potential models and heuristic constructs based on Born-Haber thermochemical cycles.

3.1. Oxide properties that influence inner sphere O_2 activation transition state energies

In inner sphere routes, O_2 reacts with O-vacancies (*) to form bound peroxo (OO*) species (step 1; Scheme 1). This step involves the transfer of two electrons from a POM cluster containing an O-vacancy (*) to a weakly-bound O_2. The minimum energy path (MEP) for this step is shown in Fig. 2 for the specific case of an O-vacancy formed in a $H_3PMo_{12}O_{40}$ cluster by removing an O-atom at O_1 location (in Fig. 1); this MEP was obtained from the triplet and spin-polarized singlet PES calculated from the NEB calculations (Fig. S.3; SI). These energies reflect DFT-derived electronic energies of structures along the inner sphere O_2 activation reaction coordinate referenced to those for the * and O_2(g) reactants.

The highest energy point along the inner sphere O_2 activation reaction coordinate is located on the triplet PES and reflects the energy of the TS_{in} that mediates the first-electron transfer step in the inner sphere routes (Fig. 2). The O-O bond distance in TS_{in} (0.125 nm; ii; Fig. 2) is very similar to that in O_2(g) molecules (0.123 nm), indicative of a reactant-like TS that occurs very early along the reaction coordinate. This first-electron transfer TS (TS_{in}) leads to the formation of an η^1-superoxo intermediate product (iii; Fig. 2) with an O-O bond distance of 0.132 nm. These superoxo species benefit from spin-orbit coupling effects [26], which lead to an energy in the broken-symmetry state (spin-polarized singlet) that is slightly lower than in either their triplet (by 3 kJ mol^{-1}) or spin-restricted singlet (by 9 kJ mol^{-1}) states. The second electron transfer leads to the formation of the η^2-peroxo product (iv; Fig. 2) with an O-O bond distance of 0.143 nm. These peroxo species are much more stable in the spin-restricted singlet state than the triplet state (Fig. 2), consistent with the pairing of all electrons in the O_2-moiety upon the transfer of two electrons from the POM cluster with a two-electron reduced center; their energies in the spin-restricted and spin-polarized singlet states differ by <1 kJ mol^{-1}.

The electronic energies of the first-electron transfer transition state (TS_{in}) involved in inner sphere O_2 activation routes (step 1; Scheme 1) are calculated for O-vacancies that are formed by removing O-atoms at different locations in POM clusters (O-atom locations and POM compositions in Fig. 1). For all O-vacancies examined, the energies and structures of TS_{in} resemble those of their respective reactant states (* and O_2), leading to TS_{in} formation energies from the reactant state of * and O_2(g) (and thus activation

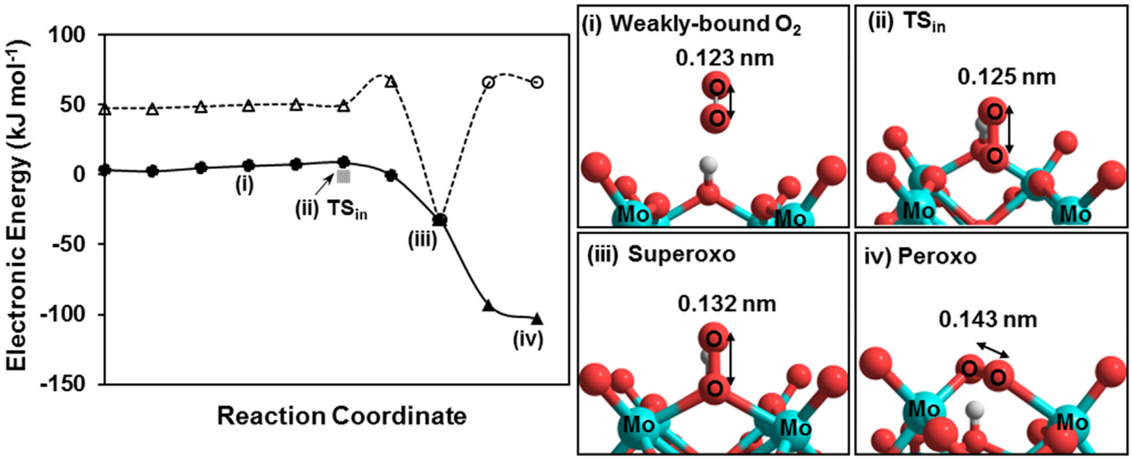

Fig. 2. The minimum energy path (MEP) derived from triplet (●) and spin-polarized singlet (▲) potential energy surfaces (PES) for the inner sphere O_2 activation routes (step 1; Scheme 1). The single-point energies of each optimized structure are also calculated and shown as open symbols for triplet (○) and spin-polarized singlet (△). The energy of TS_{in}, obtained from Dimer calculations in triplet state, is shown as a square symbol (■). The energies are calculated at an O-vacancy formed at O_1 location in $H_3PMo_{12}O_{40}$ (Fig. 1), referenced to the reactant state of * and O_2(g). Geometries of structures (i to iv) with O-O distances are shown on the right panels.

energies) that are nearly zero (ΔE_{in}^{TS} = −5 to +6 kJ mol^{-1}; Fig. 3). The O-O distances in these TS_{in} structures are also nearly unperturbed (0.123–0.130 nm; Fig. S4; SI) from those in their reactant states (O_2(g) ; 0.123 nm), consistent with the very early nature of these transition states (TS_{in}) for all O-atom locations and compositions. These O-atom locations and POM compositions cover the very broad range of O-atom properties prevalent in transition metal oxides with octahedral structures, which represent the predominant structures in practical redox-active oxides. Such early transition states are expected from Hammond's postulate [46] for very exothermic events, such as inner sphere O_2 activation steps (step 1; Scheme 1); the energies involved in forming OO* species from * and O_2(g) (ΔE_{in}^{0}) range between −76 and −259 kJ mol^{-1}, depending on the location and the composition of the POM clusters, at which the O-atoms are removed to form O-vacancies (Fig. 3).

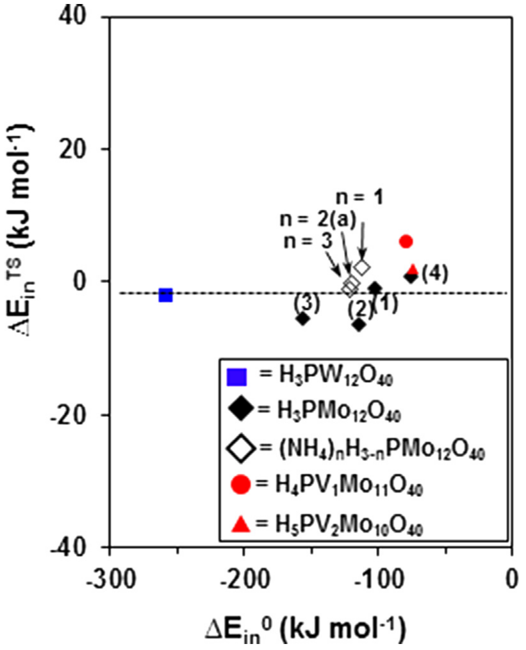

Fig. 3. DFT-derived activation barriers (ΔE_{in}^{TS}) as a function of reaction energies (ΔE_{in}^{0}) for the inner sphere O_2 activation routes (step 1; Scheme 1). These energies are referenced to the reactant state of * and O_2(g). The POM compositions and the corresponding symbols are shown in the legend. O_1-atoms (in Fig. 1) are removed from these clusters to form * centers, except for $H_3PMo_{12}O_{40}$ (◆), for which the O-vacancy locations are shown inside the parenthesis close to the data point. The numbers of NH_4^+ (n = 1, 2, 3; Fig. 1) in $(NH_4)_nH_{3-n}PMo_{12}O_{40}$ clusters are shown next to the corresponding data. Two protons vicinal to the O_1 location are substituted with NH_4^+ in the $(NH_4)_2H_1PMo_{12}O_{40}$(a) cluster (denoted as n = 2(a); Fig. 1). A dashed line represents the trend line.

These findings, in turn, show that the dynamics of inner sphere routes are essentially unaffected by the thermodynamics of the O_2 activation step, as shown by the results in Fig. 3. Consequently, the identity and binding properties of the O-atoms removed do not detectably influence the electronic energies of inner sphere O_2 activation transition states (E_{in}^{TS}). These E_{in}^{TS} values are used to calculate their free energies at relevant conditions later (Section 3.4) in order to determine the inner and outer sphere rate ratios using Eq. (7). The oxide properties that are responsible for the rates of the alternate outer sphere activation routes are discussed next.

3.2. Descriptions of outer sphere O_2 activation transition state energies in terms of oxide descriptors using crossing potential models and thermochemical cycles

H_2O dissociation on O-vacancies (*) forms vicinal OH pairs (H/OH*) (step 2; Scheme 1), adding two H-atoms on a specific O-atom pair, which includes one O-atom that is added on the O-vacancy upon H_2O adsorption and the other one chosen as the one that exhibits the most favorable energy upon H-atom addition among the six vicinal O-atoms. The resulting vicinal hydroxyls (H/OH*) then can react with O_2(g) to form H_2O_2(g), leaving the vicinal lattice O-atoms behind. Such outer sphere routes (step 3; Scheme 1) effect the oxidation of one isolated two-electron reduced center using a four-electron oxidant in the form of a dioxygen molecule.

Fig. 4a shows the mimimum energy path (MEP) for such steps at an OH pair (H/OH*) formed by H_2O dissociation on a vacancy at the O_1-location in the $H_3PMo_{12}O_{40}$ POM cluster; the MEP was calculated by combining the triplet and spin-polarized singlet PES derived from NEB calculations (Fig. S.5; SI). These energies reflect electronic energies from DFT method, referenced to the H/OH* and O_2(g) reactants involved in step 3 (Scheme 1). The highest energy point in these outer sphere O_2 activation events corresponds to the TS for the first H-atom transfer step ($TS_{out,1}$; Fig. 4ii) from H/OH* to a weakly bound O_2 by cleaving the weaker

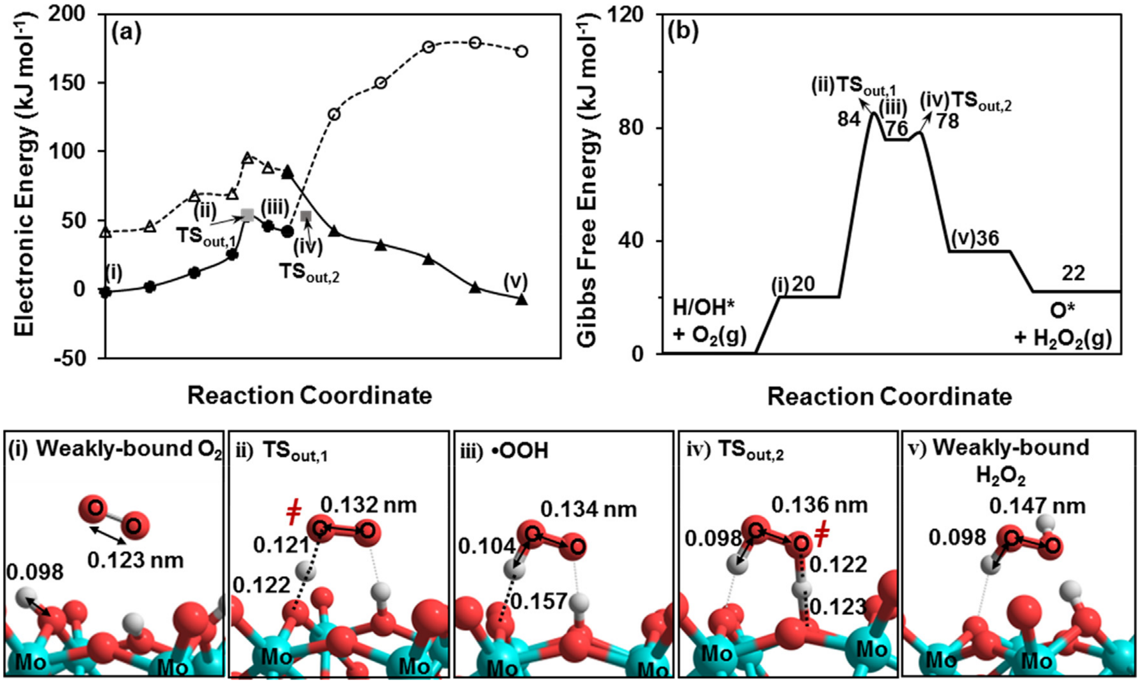

Fig. 4. (a) The minimum energy path (MEP) derived from triplet (●) and spin-polarized singlet (▲) potential energy surfaces (PES) for the outer sphere O_2 activation routes (step 3; Scheme 1). The single-point energies of each optimized structure are also calculated and shown as open symbols for triplet (○) and spin-polarized singlet (△). The TS energies for the first and second H-atom transfer steps ($TS_{out,1}$ and $TS_{out,2}$), obtained from Dimer calculations, are shown as a square symbol (■); these TS energies are derived in triplet ($TS_{out,1}$) and in spin-polarized singlet ($TS_{out,2}$) configurations. The panel (b) shows DFT-derived free energies (kJ mol^{-1}; 453 K; 1 bar O_2) of each intermediate and transition state. The energies are calculated at a H/OH* center formed via H_2O dissociation on a vacancy at O_1 location in $H_3PMo_{12}O_{40}$ (Fig. 1), referenced to the reactant state of H/OH* and O_2(g). Geometries of structures (i to v) with O-O and O-H distances are shown on the bottom panels (i-v).

O-H bond in H/OH*. This TS leads to the formation of ·OOH species interacting with a POM that contains a one-electron reduced center in the form of the remaining bound OH group (Fig. 4iii). The product of this first H-atom transfer step is more stable in its triplet state; it contains one unpaired electron in the ·OOH p-orbital and the other one in the d-orbital of the addenda atom in the POM cluster, as illustrated by spin density maps (Fig. S.6a; SI). The remaining bound OH is then cleaved and its H-atom is transferred to the interacting ·OOH to form H_2O_2 product (Fig. 4v). The weakly-bound H_2O_2 molecule formed (Fig. 4v) is much more stable in its spin-restricted singlet than its triplet state (by 180 kJ mol^{-1}), consistent with electron pairing in ·OOH p-orbitals upon transfer of the second H-atom; the energies of a weakly bound H_2O_2 in spin-restricted and spin-polarized singlet states are essentially the same (<1 kJ mol^{-1}). The triplet-singlet spin crossing occurs at the second H-atom transfer TS ($TS_{out,2}$; Fig. 4iv), which was isolated using Dimer methods in a broken-symmetry configuration (spin-polarized singlet) using the structure present at this crossing-point, obtained from the NEB calculations, as the starting point.

The MEP in Fig. 4a shows that outer sphere routes involve the formation of H_2O_2(g) via a sequential transfer of two H-atoms from H/OH* to O_2(g). The kinetic relevance of the first and second H-atom transfer steps depends on the magnitude of their rate constants and their consequences on the outer sphere O_2 activation rates (r_{out}). The pseudo-steady state concentration of ·OOH species ([·OOH]), the product of the first H-atom transfer step, is given by the ratio of their formation rate via the first H-atom transfer to the rate constants for their disappearance via either the reverse reaction of the first H-atom transfer ($k_{out,-1}$) to re-form a weakly-bound O_2 on H/OH* or the second H-atom transfer to form a weakly-bound H_2O_2 on an O-atom pair ($k_{out,2}$):

$$[\cdot OOH] = \frac{k_{out,1}P_{O_2}[H/OH*]}{k_{out,-1} + \ k_{out,2}} \tag{8}$$

Here, [H/OH*] represents the surface coverage of vicinal OH pairs. $k_{out,1}$ is the first-order rate constant for the first H-atom transfer step, which depends on the free energy difference between the first-H-atom transfer TS ($TS_{out,1}$;Fig. 4ii) and H/OH* and O_2(g). The values of $k_{out,-1}$ and $k_{out,2}$ reflect, in turn, the free energies for the first and second H-atom transfer transition states ($TS_{out,1}$ and $TS_{out,2}$; Fig. 4ii and iv), respectively; both are referenced to the ·OOH intermediate interacting with the POM with one OH group (Fig. 4iii). The [·OOH] concentration given by Equation (8) leads to the rate for the outer sphere O_2 activation routes (step 3; Scheme 1), given by:

$$r_{out} = \frac{k_{out,1}k_{out,2}}{k_{out,-1}+k_{out,2}}P_{O_2}[H/OH*] \tag{9}$$

The accurate assessment of these rate constants requires the estimation of free energies at the relevant reaction conditions (453 K; 1 bar O_2), which are shown in Fig. 4b for a specific H/OH* center (at the O_1 location in a $H_3PMo_{12}O_{40}$ POM cluster) as an illustrative example. A O_2 molecule weakly interacts with a H/OH* center (ΔG_{ads} = +20 kJ mol^{-1}; Fig. 4b). The transfer of the first H-atom from H/OH* to a weakly-bound O_2 molecule form a ·OOH intermediate and an isolated OH center; the TS for this step leads to a free energy barrier of 64 kJ mol^{-1} ($TS_{out,1}$; Fig. 4b; ii). The second H-atom is transferred to the ·OOH intermediate via a kinetically-irrelevant step with a very small free energy barrier (+2 kJ mol^{-1}; $TS_{out,2}$; Fig. 4b; iv), which appears as a downhill "ledge" along the reaction coordinate to form a weakly-bound H_2O_2. The H_2O_2 formed desorbs in an exoergic step (ΔG_{des} = -14 kJ mol^{-1}; Fig. 4b; v). DFT-derived free energies calculated for this specific H/OH* center (at the O_1 location in $H_3PMo_{12}O_{40}$) indicate that the free energy barrier for the second H-atom transfer step from the ·OOH intermediate (+2 kJ mol^{-1}; $TS_{out,2}$; Fig. 4b; iv) is smaller than that required to re-from the weakly-bound O_2 via the reverse of the first H-atom transfer step (+8 kJ mol^{-1}; TS$_{out,1}$; Fig. 4b; ii); thus, the ($k_{out,-1}/k_{out,2}$) rate constant ratio in Eq. (9) calculated at this location is smaller than unity (0.2), suggesting that the first H-atom transfer step controls the outer sphere O_2 activation rates.

This specific H/OH* center (at O_1 location in $H_3PMo_{12}O_{40}$), shown as an illustrative example in Fig. 4b, exhibits the most endothermic reaction energy for the first H-atom transfer step ($\Delta E_{out,1}{}^0$) among the H/OH* centers examined in this work (Fig. 5a); here, only the electronic component of the reaction energies is compared. The first H-atom transfer step ($\Delta E_{out,1}{}^0$) becomes less endothermic and then exothermic, as the POM composition changes from $H_3PMo_{12}O_{40}$ to $(NH_4)_3PMo_{12}O_{40}$, and to $H_3PW_{12}O_{40}$ (+42 to 0 and −38 kJ mol^{-1}; for the H/OH* centers at the same O_1 location; Fig. 5a). Accordingly, the ($k_{out,-1}/k_{out,2}$) ratio decreases from 0.2 to 0.02 and to 1×10^{-5}. These trends indicate, in turn, that the ($k_{out,-1}/k_{out,2}$) ratios would be much smaller than unity ($\ll 0.2$) at all other H/OH* centers that exhibit less endothermic or exothermic $\Delta E_{out,1}{}^0$ energies than the specific H/OH* (at O_1 location in $H_3PMo_{12}O_{40}$) shown in Fig. 4b and that the outer sphere rates are controlled by the first H-atom transfer step ($k_{out,1}$ in Eq. (9)) for the range of O-atoms examined in this work.

The $k_{out,1}$ parameter (in Eq. (9)) reflects the free energy of the first H-atom transfer TS (TS$_{out,1}$; Fig. 4ii), referenced to its H/OH* and $O_2(g)$ precursors. The specific binding properties of oxides that determine these TS$_{out,1}$ energies are discussed next using crossing-potential models and thermochemical cycles. Here, we restrict the analysis to the electronic energies of these transition states ($E_{out,1}$), but ZPVE corrections and thermal contributions of enthalpy and entropy are included to give free energies in Section 3.4 in order to accurately assess the relative rates of inner and outer sphere routes and their most accurate descriptors.

3.2.1. Crossing-potential description of the lateness of transition states

The structures and energies of the first H-atom transfer TS (TS$_{out,1}$) in outer sphere O_2 activation routes (step 3; Scheme 1) were determined for H/OH* centers that are formed via H_2O dissociation on O-vacancies at different locations in compositionally-diverse POM clusters (the range of O-atom locations and POM compositions in Fig. 1). The structure of TS$_{out,1}$ at the H/OH* center in a $H_3PW_{12}O_{40}$ cluster (formed at a vacancy created by the removal of the O_1 atom) closely resembles that of the reactant state (H/OH* and $O_2(g)$); the O-H bond at TS$_{out,1}$ is nearly unperturbed from the reactant H/OH* (0.098 nm in H/OH* vs. 0.103 nm at TS$_{out,1}$; Fig. 6) and not yet formed at the ·OOH product (0.157 nm at TS$_{out,1}$ vs. 0.104 nm in ·OOH; Fig. 6). The first H-atom transfer step ($\Delta E_{out,1}{}^0$) becomes less exothermic and then increasingly endothermic, as the POM composition changes from $H_3PW_{12}O_4$ to $(NH_4)_1H_2PMo_{12}O_{40}$ and to $H_3PMo_{12}O_{40}$ (from −38 to +17 and +42 kJ mol^{-1} for the H/OH* centers at the same O_1 location; Fig. 5a). Accordingly, TS$_{out,1}$ structures more closely resemble the product states; the surface O-H bonds at TS$_{out,1}$ are increasingly elongated (0.103, 0.108 and 0.122 nm; Fig. 6) from the reactant state of H/OH* (0.098 nm) and formed the ·OOH moiety (0.157, 0.143, 0.121 nm; Fig. 6), approaching that in the product ·OOH state (0.104 nm).

These trends reflect changes in the location of TS$_{out,1}$ along the O_2 activation reaction coordinate. The "lateness" of TS $_{out,1}$ (η) can be defined as the extent of the elongation of surface O-H bond at TS$_{out,1}$ (Δ(O-H)^{TS}) relative to that in the ·OOH···O* product state (Δ(O-H)^0):

$$\eta = \frac{\Delta(O-H)^{TS}}{\Delta(O-H)^{0}} = \frac{(O-H)_{OH*}{}^{TS} - (O-H)_{OH*}}{(O-H)_{\cdot OOH--O*}{}^{0} - (O-H)_{OH*}} \qquad (10)$$

Here,$(O-H)_{OH*}$, $(O-H)_{OH*}{}^{TS}$ and $(O-H)_{\cdot OOH\cdots O*}{}^{0}$ represent the bond distances between the surface O-atom and the H-atom (that is transferred during the first H-atom transfer) at the reactant (H/OH*), TS$_{out,1}$, and product (·OOH--O*) states.

The η value increases as the reaction energy ($\Delta E_{out,1}{}^0$) becomes less negative and then increasingly positive (Fig. 5b), bringing the

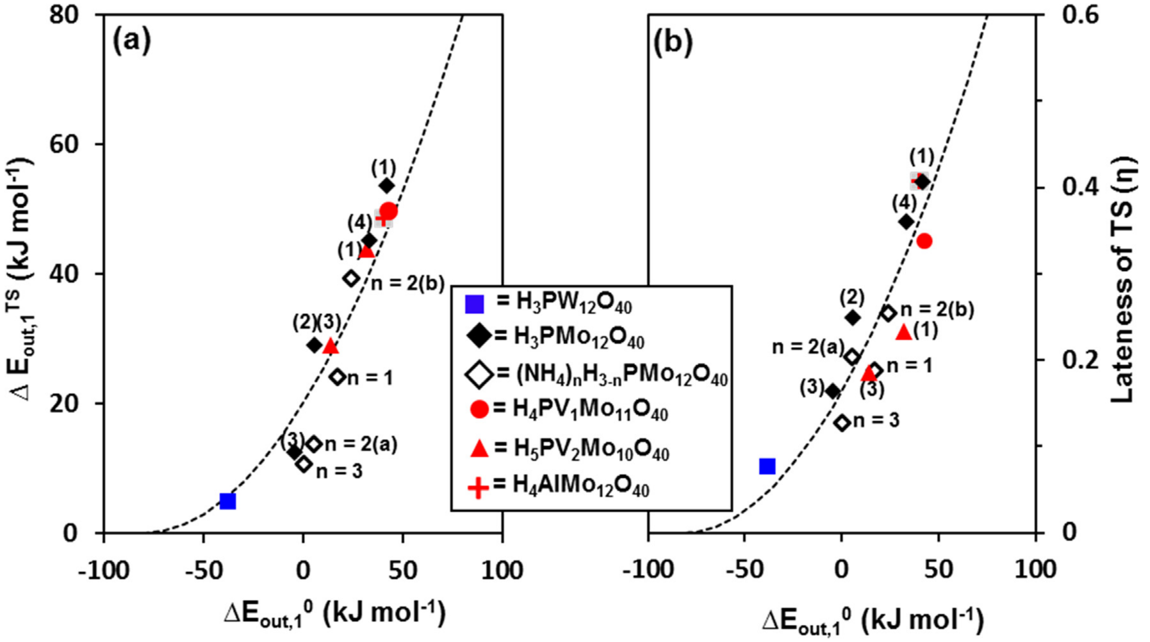

Fig. 5. (a) DFT-derived activation barriers for the first H-atom transfer step (TS$_{out,1}$) in the outer sphere O_2 activation routes (step 3; Scheme 1) and (b) the "lateness" of TS$_{out,1}$ (η; Eq. (10)) as a function of respective reaction energies ($\Delta E_{out,1}{}^0$). The energies are referenced to the reactant states of H/OH* and $O_2(g)$. The POM compositions and the corresponding symbols are shown in the legend. These calculations involve H/OH* centers at O_1 location (Fig. 1), except for $H_3PMo_{12}O_{40}$ (◆) and $H_5PV_2Mo_{10}O_{40}$ (▲) clusters, for which the O-vacancy locations are shown inside the parentheses near the data symbols. The numbers of NH_4^+ (n = 1,2,3) in $(NH_4)_nH_{3-n}PMo_{12}O_{40}$ clusters are shown next to the corresponding data. For the $(NH_4)_2H_1PMo_{12}O_{40}$ clusters, two protons vicinal or distant to the O_1 location are substituted with NH_4^+ (denoted as n = 2(a) and 2(b) in the figure; Fig. 1). The dashed curves reflect the best regression fit of the data to the functional form of Equation (11) in panel (a) and a trend line in panel (b).

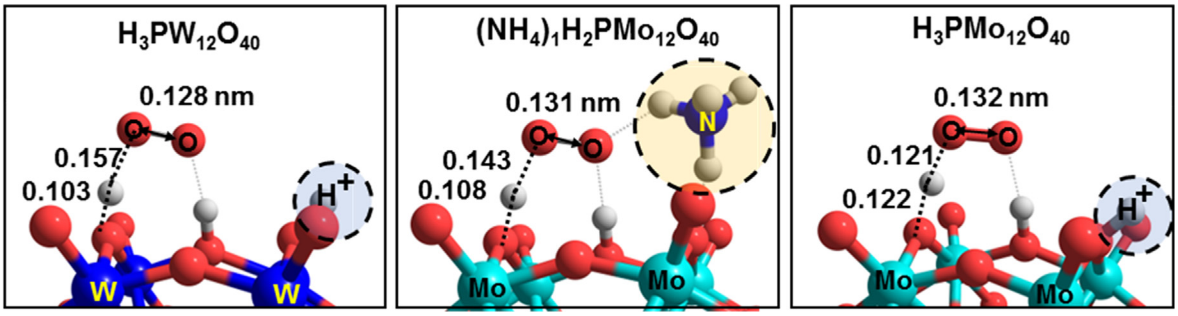

Fig. 6. DFT-derived structures of the first H-atom transfer transition states ($TS_{out,1}$) in the outer sphere O_2 activation routes (step 3; Scheme 1) for the H/OH* centers at O_1 location in $H_3PW_{12}O_{40}$, $(NH_4)_1H_2PMo_{12}O_{40}$ and $H_3PMo_{12}O_{40}$ clusters. The charge-balancing cations (H^+ and NH_4^+) are highlighted using dashed circles. The O-H and O-O bond distances are in units of nm.

structure and energy of $TS_{out,1}$ closer to those in the product state of the first H-atom transfer step. Such shifts in their locations along the reaction coordinate render $TS_{out,1}$ energies to become more sensitive to the stability of the product states and thus to the properties of the O-atoms at oxide surfaces, as this elementary step becomes thermodynamically less favorable. Such trends are also evident in the curvature of the scaling relations between the activation barriers and reaction energies ($\Delta E_{out,1}{}^{TS}$ and $\Delta E_{out,1}{}^{0}$; Fig. 5a). As the elementary step becomes very endothermic, the sensitivity of activation energies to their thermodynamics ultimately reaches a slope of unity (Fig. 5a), consistent with Hammond's postulate [46].

These ubiquitous non-linear scaling relations can be accurately captured by describing the transition state at the crossing point between two harmonic potentials [47,48]; in this case, these potentials correspond to the two O-H bonds, the one cleaved in H/OH* and the other formed in ·OOH (Scheme 2). In such constructs, the energy of formation of a $TS_{out,1}$ ($\Delta E_{out,1}{}^{TS}$) from its reactant state (H/OH* and O_2(g)) is given in terms of the respective reaction energy ($\Delta E_{out,1}{}^{0}$) [26,47,48];

$$\Delta E_{out,1}{}^{TS} = \frac{\left(\lambda + \Delta E_{out,1}{}^{0}\right)^2}{4\lambda} \tag{11}$$

Here, λ represents the energy of the O-H bond in the ·OOH product state at the minimum energy point of the potential curve for the O-H bond in the H/OH* reactant state (Scheme 2); its magnitude depends on the type of bonds being cleaved and made in any given reaction, which is similar for the systems of interest here. The data in Fig. 5a give a λ value of 81 ± 8 kJ mol^{-1} (the uncertainties reflect standard errors) when regressed to the functional form of Eq. (11); the regressed fit is shown as the dashed curve in Fig. 5a, which accurately captures the data for all H/OH* centers at different locations and POM compositions. The functional relation between $\Delta E_{out,1}{}^{TS}$ and $\Delta E_{out,1}{}^{0}$ in Eq. (11) is used next together with the thermochemical cycle shown in Scheme 3 to relate the outer sphere O_2 activation reactivities, through the stability of the $TS_{out,1}$ structures, to the properties of molecules and oxide surfaces that determine the formation energies of ·OOH species from H/OH* and O_2(g) ($\Delta E_{out,1}{}^{0}$), the reactant state for step 3 in Scheme 1.

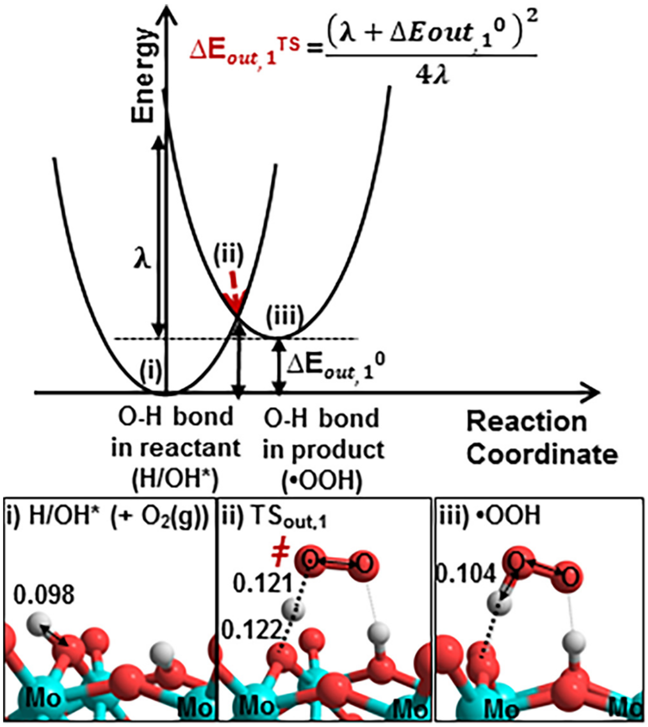

Scheme 2. Crossing potential model used to relate the activation energies ($\Delta E_{out,1}{}^{TS}$) to the reaction energies ($\Delta E_{out,1}{}^{0}$) for the first H-transfer step in the outer sphere routes (step 3; Scheme 1). The TS for the first H-atom transfer step ($TS_{out,1}$) is described by the crossing point of two O-H potentials, each of which belongs to the reactant (H/OH*) and to the product (·OOH radical), respectively. Geometries of (i) H/OH* (ii) $TS_{out,1}$, and (iii) ·OOH radical interacting with the POM cluster with a OH* center are shown for the H/OH* center at O_1 location in $H_3PMo_{12}O_{40}$ (Fig. 1); the O-H bond distances in each of the structures are in units of nm.

3.2.2. Born-Haber thermochemical cycles that dissect reaction energies into molecular and catalytic properties

Reaction energies for the first H-atom transfer step in outer sphere O_2 activation routes ($\Delta E_{out,1}{}^{0}$; step 3; Scheme 1) can be described using three hypothetical steps (shown in Scheme 3). These steps are: (i) the cleavage of the weaker O-H bond in the bound OH pair (H/OH*) to form H(g) and a bound OH (the negative of the second H-atom addition energy, -HAE_2); (ii) the reaction of H(g) with O_2(g) to form ·OOH(g) in a step that is unaffected by any properties of the catalytic surfaces (·OOH(g) formation energy; E_{OOH}); and (iii) the placement of ·OOH(g) into the contact with the POM cluster containing the bound OH center (the interaction energy at the product state; $E_{int}{}^{0}$).

The reaction energy is then rigorously given by the energies of the three hypothetical steps in Scheme 3:

$$\Delta E_{out,1}{}^{0} = E_{OOH} + E_{int}{}^{0} - HAE_2 \tag{12}$$

This equation, taken together with Eq. (11), describes the energy of formation of a $TS_{out,1}$ from its H/OH* and O_2(g) precursors ($\Delta E_{out,1}{}^{TS}$):

$$\Delta E_{out,1}{}^{TS} = \frac{\left(\lambda + E_{OOH} + E_{int}{}^{0} - HAE_2\right)^2}{4\lambda} \tag{13}$$

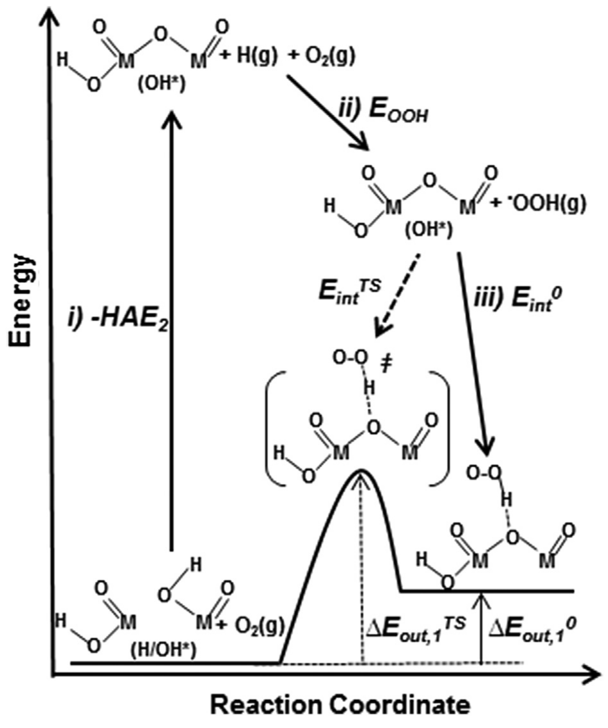

Scheme 3. A thermochemical cycle describing the first H-transfer step in the outer sphere O_2 activation routes (step 3; Scheme 1). This step involves the O_2(g) reaction with H/OH* to form ·OOH radical interacting with the POM with a OH* center. The reaction energies ($\Delta E_{out,1}{}^0$) are expressed as a sum of the energies for (i) the cleavage of the weaker O-H bond in H/OH* to form H(g) and a OH* center (−HAE$_2$), (ii) the addition of this H(g) to O_2(g) to form ·OOH(g) (E_{OOH}), and (iii) the interaction between ·OOH(g) and the surface at the product state (E^0_{int}).

This equation relates the $\Delta E_{out,1}{}^{TS}$ value to the intrinsic thermodynamic properties of oxide surfaces (HAE$_2$ and $E_{int}{}^0$); the E_{OOH} and λ values in this equations are set by the properties of molecules and the type of reaction, but they do not sense any binding properties of the oxide surfaces.

Fig. 7a shows activation barriers for the first H-atom transfer step ($\Delta E^{TS}_{out,1}$) in the outer sphere O_2 activation routes (step 3; Scheme 1) as a function of HAE$_2$ for each specific H/OH* location and POM composition; its negative value (-HAE$_2$) reflects the energy required to cleave the weaker O-H bond in H/OH* centers (step i; Scheme 3). The OH species in the H/OH* centers that require larger energy to cleave their O-H bonds (more negative HAE$_2$) impose larger $\Delta E^{TS}_{out,1}$ barrier (Fig. 7a) because these O-H bonds become preferentially cleaved in forming the ·OOH products and thus are elongated at $TS_{out,1}$. The $\Delta E_{out,1}{}^{TS}$ value increases as HAE$_2$ becomes more negative but such trend weakens as HAE$_2$ becomes less negative (Fig. 7a) and the reaction becomes less endothermic (and ultimately more exothermic). These changes reflect $TS_{out,1}$ structures that appear earlier along the reaction coordinate (η; Fig. 5b) and become less sensitive to the energy of the reaction step and thus to the binding properties of surfaces.

The $\Delta E_{out,1}{}^{TS}$ barriers calculated for all H/OH* centers lie along a single trend curve in Fig. 7a, except for those vicinal to a large charge-balancing cation, NH_4^+ (at O_1 location in $(NH_4)_1H_2PMo_{12}O_{40}$, $(NH_4)_2H_1PMo_{12}O_{40}$(a) and $(NH_4)_3PMo_{12}O_{40}$ clusters). The data for these H/OH* centers non-vicinal to NH_4^+ cations (in Fig. 7a) give a value of ·OOH-surface interaction energy ($E_{int}{}^0$ = −50 ± 2 kJ mol^{-1}; the uncertainties represent standard errors) when regressed to the functional form of Eq. (13) (with λ = 81 ± 8 kJ mol^{-1}, estimated in Section 3.2.1). The regressed fit accurately captures the $\Delta E_{out,1}{}^{TS}$ barriers for all H/OH* centers that do not involve vicinal NH_4^+

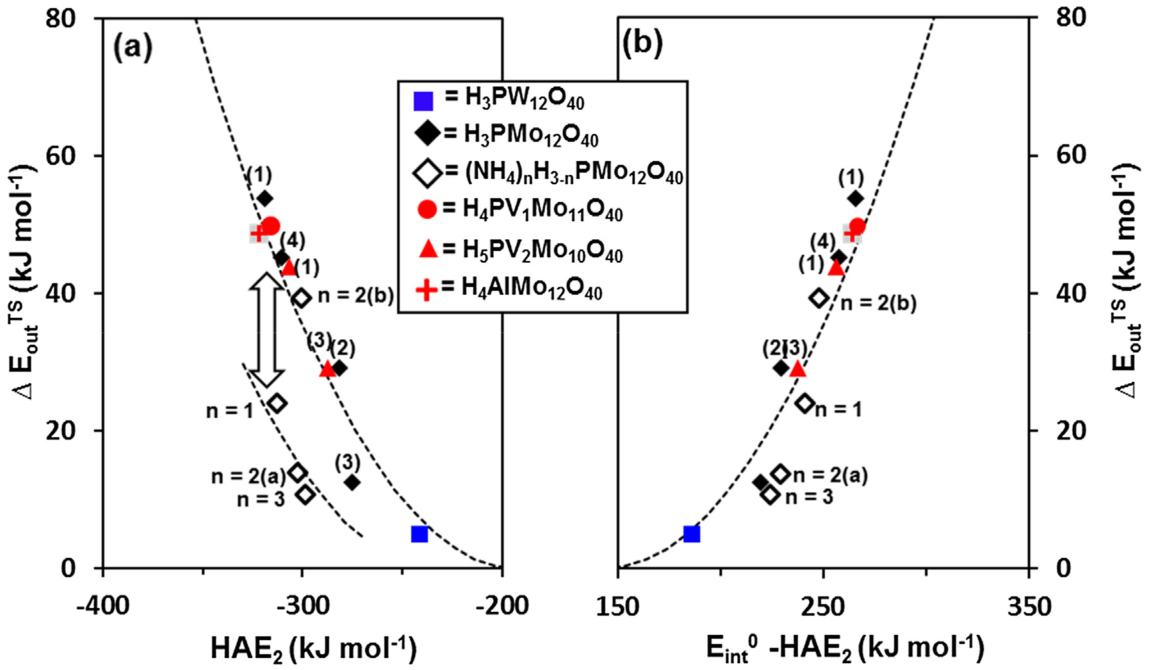

Fig. 7. DFT-derived activation barriers ($\Delta E_{out,1}{}^{TS}$) for the first H-atom transfer step in the outer sphere O_2 activation routes (step 3; Scheme 1) as a function of (a) the second H-atom addition energy (HAE$_2$) and of (b) the summated energies of the negative value of HAE$_2$ and ·OOH-surface interaction energies at the product states ($E_{int}{}^0$-HAE$_2$). The POM compositions and the corresponding symbols are shown in the legend. These calculations involve H/OH* centers formed at O_1 location (in Fig. 1), except for $H_3PMo_{12}O_{40}$ (◆) and $H_5PV_2Mo_{10}O_{40}$ (▲) clusters, for which their locations are shown inside the parenthesis close to each data point. The numbers of NH_4^+ (n = 1,2,3) in $(NH_4)_nH_{3-n}PMo_{12}O_{40}$ clusters are shown next to the corresponding data; two protons vicinal or distant to O_1-atom are substituted with NH_4^+ in the $(NH_4)_2H_1PMo_{12}O_{40}$ clusters (denoted as n = 2(a) and 2(b) in the figure). Dashed curves represent the best fit of the data to the functional form of Eq. (13).

cations, as shown by the dashed curve in Fig. 7a, giving HAE$_2$ as a complete descriptor of oxide properties to predict the $\Delta E_{out,1}{}^{TS}$ barriers for such H/OH"* centers.

The $E_{int}{}^{0}$ values can also be independently assessed at each H/OH* center by calculating the energy released upon bringing ·OOH(g) to its interaction distance to the POM cluster that contains the residual isolated OH* center; these values are shown in Fig. 8 as a function of HAE$_2$. All H/OH* centers in compositionally-diverse POM clusters exhibit similar interaction energies at the product state of the first H-atom transfer step ($E_{int}{}^{0}$; −58 to −50 kJ mol^{-1}; Fig. 8), in spite of their very different HAE$_2$ values (−322 to −242 kJ mol^{-1}; Fig. 8), as long as these H/OH* centers are distant from large charge-balancing cations (e.g., NH_4^+). These $E_{int}{}^{0}$ values reflect the attractive interactions between unpaired electrons in ·OOH p-orbitals and in the d-orbitals of POM addenda atoms; these spin pairs act as molecular magnets [26] in stabilizing ·OOH species. The spin distributions at the product state of the first H-atom transfer are similar among oxides, as indicated by their spin density maps (shown for H/OH* centers at O_1 location in $H_3PMo_{12}O_{40}$ and $H_3PW_{12}O_{40}$ in Fig. S6; SI), resulting in similar $E_{int}{}^{0}$ values. The similar magnitude of $E_{int}{}^{0}$ values, in turn, allows $\Delta E_{out,1}{}^{TS}$ barriers for all H/OH* centers to be described as a single-valued function of HAE$_2$, as long as they do not involve vicinal NH_4^+ cations (Fig. 7a).

The presence of a small vicinal charge-balancing cation (e.g., H$^+$) does not influence the stability of ·OOH species formed, as indicated by the similar ·OOH-surface interaction energies ($E_{int}{}^{0}$) for those formed at the H/OH* centers with and without vicinal H$^+$ ($E_{int}{}^{0}$ = −53 vs. −56 kJ mol^{-1} for H/OH* centers at O_1 and O_3 locations in $H_3PMo_{12}O_{40}$; Fig. 8). $E_{int}{}^{0}$ values also do not sense the identity of the charge-balancing cations that are distant from the H/OH* center; they remain similar as two charge-balancing protons distant from the H/OH* center (at O_1-location) in $H_3PMo_{12}O_{40}$ are replaced with NH_4^+ (−53 and −52 kJ mol^{-1} for the H/OH* centers at the same O_1 location in $H_3PMo_{12}O_{40}$ and $(NH_4)_2H_1PMo_{12}O_{40}$(b) clusters; Fig. 8).

The ·OOH species formed, however, can interact with a large vicinal charge-balancing cation, causing more negative $E_{int}{}^{0}$ values for those formed at H/OH* centers vicinal to NH_4^+ (at O_1-location in $(NH_4)_1H_2PMo_{12}O_{40}$, $(NH_4)_2H_1PMo_{12}O_{40}$(a) and $(NH_4)_3PMo_{12}O_{40}$ clusters; Fig. 8). The $E_{int}{}^{0}$ values become much more negative (from −53 to −72 kJ mol^{-1}) as the charge-balancing H$^+$ vicinal to the H/OH* center (at O_1-location) in the $H_3PMo_{12}O_{40}$ POM cluster is replaced with NH_4^+ (the $(NH_4)_1H_2PMo_{12}O_{40}$ POM cluster; Fig. 8). Distant charge-balancing cations again do not influence the $E_{int}{}^{0}$ values, which remain similar upon replacement of the remaining charge-balancing protons in $(NH_4)_1H_2PMo_{12}O_{40}$ with NH_4^+ (−73 and −75 kJ mol^{-1} for H/OH* centers at the same O_1 location in $(NH_4)_2H_1PMo_{12}O_{40}$(a) and $(NH_4)_3PMo_{12}O_{40}$ clusters; Fig. 8). The effects of charge-balancing cations on $E_{int}{}^{0}$ values depend sensitively on the identity of the cations and on their distances to the ·OOH species formed; therefore, for the accurate description of the outer sphere rates, $E_{int}{}^{0}$ must be explicitly calculated when these cations are present at vicinal locations.

Fig. 7b shows the $\Delta E_{out,1}{}^{TS}$ barriers for abstracting the first H-atom from H/OH* by O_2(g) as a function of ($E_{int}{}^{0}$-HAE$_2$), the descriptor that fully describes these barriers for all H/OH* locations, POM compositions, and charge-balancing cations. The dashed curve represents the trend dictated by the functional form of Eq. (13), which rigorously captures the lateness of TS $_{out,1}$ as it evolves with the changes in reaction energies.

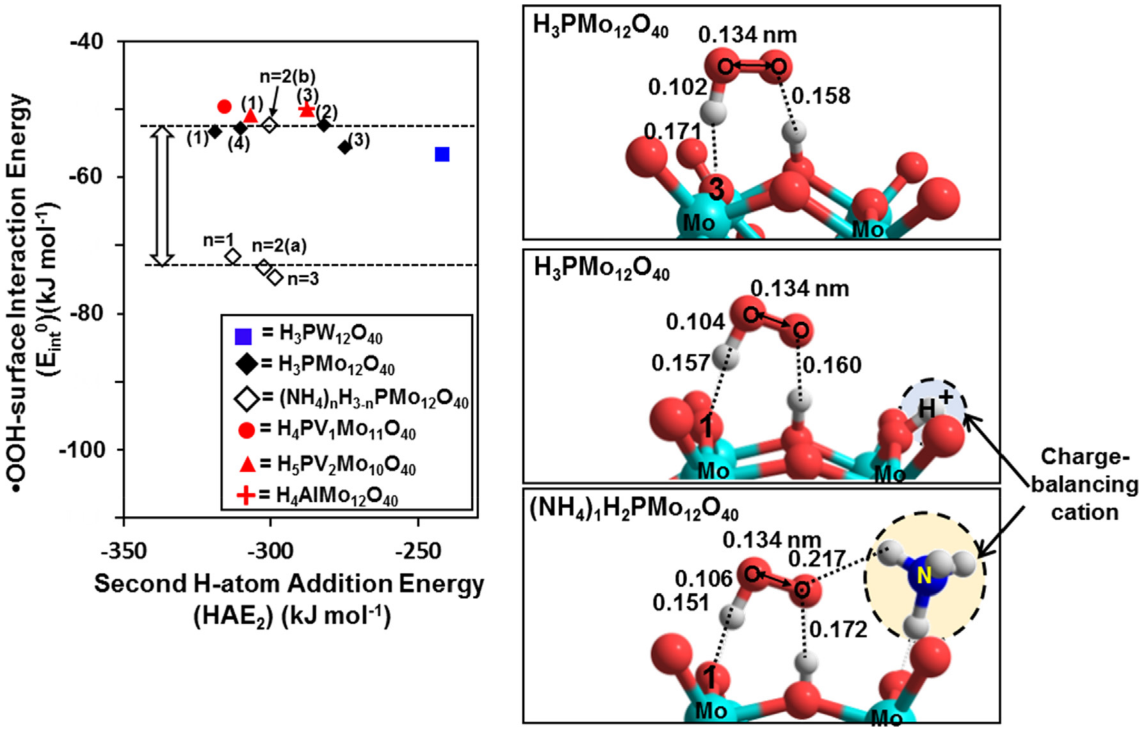

Fig. 8. DFT-derived ·OOH-surface interaction energies ($E_{int}{}^{0}$) at the products state of the first H-atom transfer step in the outer sphere routes (step 3; Scheme 1). The POM compositions and the corresponding symbols are shown in the legend. These calculations involve H/OH* centers at O_1 location (in Fig. 1), except for $H_3PMo_{12}O_{40}$ (◆) and $H_5PV_2Mo_{10}O_{40}$ (▲) clusters, for which their locations are shown inside the parenthesis close to each data point. The numbers of NH_4^+ (n = 1,2,3) in $(NH_4)_nH_{3-n}PMo_{12}O_{40}$ clusters are shown next to the corresponding data; two protons vicinal or distant to O_1-atom are substituted with NH_4^+ in the $(NH_4)_2H_1PMo_{12}O_{40}$ clusters (denoted as n = 2(a) and 2(b) in the figure). Dashed lines represent the trend lines. DFT-derived structures of interacting ·OOH species and the surface are shown in the right panels for the H/OH* centers at O_1 and O_3 locations in $H_3PMo_{12}O_{40}$ and at O_1 location in $(NH_4)_1H_2PMo_{12}O_{40}$; the O-O and O-H bond distances in each of the structures are in units of nm. The charge-balancing cations (H$^+$ and NH_4^+) are highlighted using dashed circles.

Thus far, the results and conclusions have addressed how intrinsic oxide properties influence the formation energies of inner and outer transition states (TS_{in} and $TS_{out,1}$) from their respective surface precursors (* and H/OH*) and O_2(g) (the reactant states of steps 1 and 3; Scheme 1). These reactant states (* and H/OH*), however, also differ in energy; such energy differences depend on oxide properties and influence the relative coverages of * and H/OH* and therefore the relative rates of inner and outer sphere routes.

3.3. Interconversion of O-vacancies (*) and OH pairs (H/OH*) and the thermodynamics of H_2O dissociation on isolated O-vacancies

H_2O dissociation on O-vacancies form vicinal OH pairs (H/OH*) (step 2; Scheme 1), the reactants involved in outer sphere O_2 activation routes (step 3; Scheme 1). These steps are typically in quasi-equilibrium during catalytic oxidations and lead to lower selectivity for inner sphere O_2 activation routes at higher H_2O concentrations [4]. Such * and H/OH* interconversions involve charge reorganization within the POM clusters upon the formation of M-O and O-H bonds, but no electron transfer or changes in the oxidation state of the metal centers in oxides. The O-vacancy location and the POM composition influence H_2O dissociation energies, in a manner that we explore through the formalism of Born-Haber thermochemical cycles. Here, we restrict our analysis to the effects of oxide properties on H_2O dissociation electronic energies (ΔE_{H_2O}), but the relevant free energies (Eqs. (1) and (2)) are included in the calculations of inner and outer sphere rate ratios presented later in Section 3.4.

A thermochemical cycle that conveniently separates H_2O dissociation energies on O-vacancies (step 2 in Scheme 1; ΔE_{H_2O}) is shown in Scheme 4; such a step adds two H-atoms at a specific O* pair, which consists of an O-atom that is added on an O-vacancy during H_2O adsorption and the other that is vicinal to this O-atom and presents the most stable energy upon H-atom addition among six neighboring O-atoms. This cycle consists of: (i) the dissociation of H_2O(g) into one O(g) atom and two H(g) atoms (the negative of the formation energy of gaseous water from its atoms, -E_f), a property that cannot sense the binding properties of the oxide surfaces; (ii) the addition of this O(g) to an O-vacancy (*) formed at a given location and POM composition (in Fig. 1) to form a bound lattice O-atom (O*) (the negative of the O-atom removal energy from O* to form *, -ORE); (iii) the addition of a H(g) at an O* center that forms the stronger O-H bond in the O* pair (more negative H-atom addition energy) with an energy given the first H-atom addition energy (HAE_1); and (iv) the addition of a second H(g) at the remaining O-atom in the pair to form vicinal hydroxyls (H/OH*) with an energy given by the second H-atom addition energy (HAE_2). This H-atom added in step iv forms a weaker O-H bond in the OH pair than the one added in step iii and thus is transferred first to a weakly-bound O_2 in the outer sphere route (step i; Scheme 3; Section 3.2).

The thermochemical cycle in Scheme 4 leads to H_2O dissociation energies (ΔE_{H_2O}; step 2 in Scheme 1) given by the sum of those for steps i-iv:

$$\Delta E_{H_2O} = HAE_1 + HAE_2 - ORE - E_f, \tag{14}$$

where the E_f term cannot sense the oxide properties and the other terms connect ΔE_{H_2O} values to the properties of the oxide surface, specifically the energy required to remove an O-atom (ORE) or released upon the addition of H-atoms (HAE_1 and HAE_2). The magnitude of these three energies (ORE, HAE_1 and HAE_2) may vary similarly with changes in O-atom location and POM composition, because each one involves the transfer of electrons into the LUMO of the metal oxide. If these properties are indeed inter-related, the magnitude of ΔE_{H_2O} would be accurately described by a single-valued function of any one of these energies. These ORE, HAE_1, and HAE_2 values are calculated for O-atoms at different locations in compositionally-diverse POM clusters (O-atom locations and POM compositional range depicted in Fig. 1) and are shown in Fig. 9.

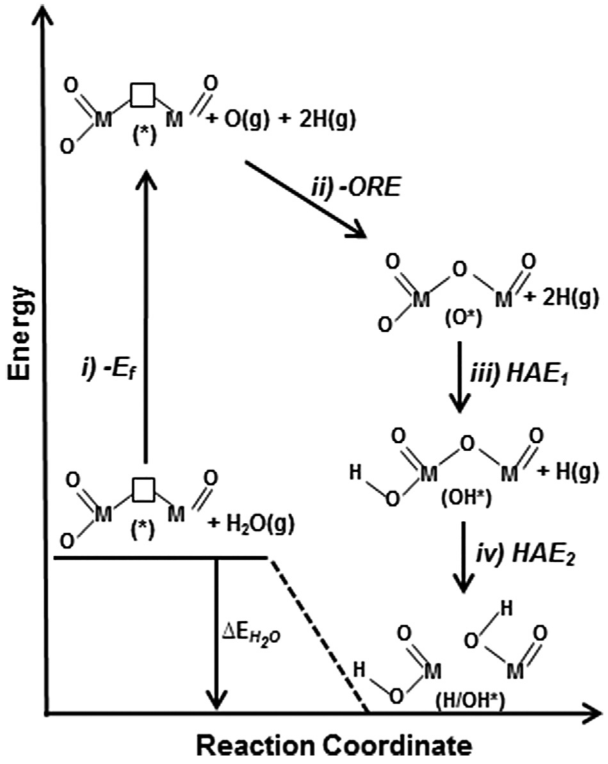

Scheme 4. A thermochemical cycle describing H_2O dissociation energies to form H/OH* on * (ΔE_{H_2O}; step 2; Scheme 1) ^{a}This cycle includes (i) the dissociation of H_2O(g) into one O(g) and two H(g) (the negative value of H_2O formation energy from its atoms, $-E_f$); (ii) the addition of this O(g) on * to reform O* (the negative value of O-atom removal energy from O* to form *, -ORE), (iii) the addition of the first H(g) on an O* center that forms stronger O-H bond between the two O-atoms in the O* pair (the first H-atom addition energy, HAE_1); (iv) the addition of the second H(g) on the remaining O-atom in the pair to form a OH pair (the second H-atom addition energy, HAE_2).

3.3.1. Intrinsic relations between the oxygen removal (ORE) and the two H-addition (HAE_1 + HAE_2) energies

ORE values scale linearly with the sum of the energies associated with the sequential addition of two H-atoms ($HAE_1 + HAE_2$), one at the O-atom removed in determining ORE and the other at the vicinal O-atom with the most negative HAE; the slope of this linear relation is 1.22 ± 0.04 for the range of O-atom locations and POM compositions described in Fig. 1, with ORE values that become smaller as ($HAE_1 + HAE_2$) values become more negative (Fig. 9a). This trend is expected between the two two-electron reduction processes, one involving the removal of one O-atom and the other the addition of two H-atoms, for which the energies of the processes vary in concert with O-atom location and POM composition. These two energies (ORE and $HAE_1 + HAE_2$) depend on specific properties of the oxides that are examined next by dissecting the two processes into convenient constitutive steps using Born-Haber thermochemical cycles (Schemes 5a and b).

ORE values equal the sum of energies for: (i) removing an O^{2-} anion from a neutral POM cluster to create an O-vacancy and a POM cluster with a 2+ charge ($(POM_*)^{2+}$); (ii) removing two electrons from the gaseous O^{2-} anion to form O(g) and two electrons (the negative of the sum of the first and second electron affinity

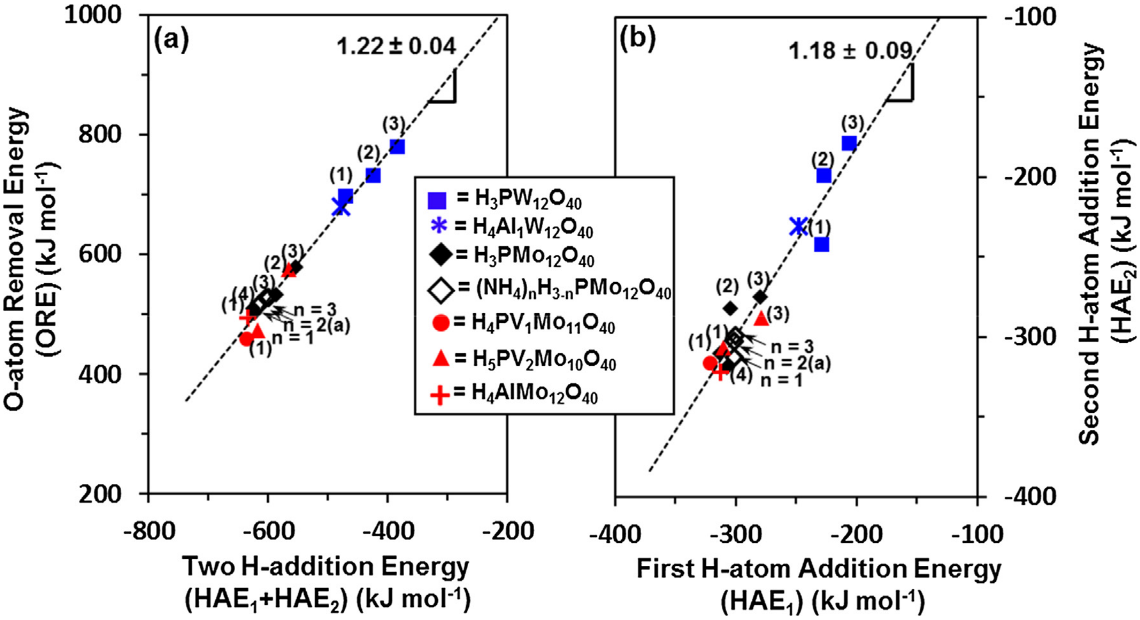

Fig. 9. (a) DFT-derived O-atom removal energies (ORE; step ii; Scheme 4) as a function of the two H-addition energies ($HAE_1 + HAE_2$; steps iii and iv; Scheme 4) and (b) the second H-atom addition energies (HAE_2; step iv; Scheme 4) as a function of the first H-atom addition energies (HAE_1; step iii; Scheme 4). The POM compositions and the corresponding symbols are shown in the legend. These values are calculated at O_1 location (in Fig. 1), except for $H_3PW_{12}O_{40}$ (■), $H_3PMo_{12}O_{40}$ (◆), and $H_5PV_2Mo_{10}O_{40}$ (▲) clusters, for which O-atom locations are shown inside the parenthesis close to each data point. The numbers of NH_4^+ (n = 1,2,3) in $(NH_4)_nH_{3-n}PMo_{12}O_{40}$ clusters are shown next to the corresponding data; two protons vicinal the O_1-atom are substituted with NH_4^+ in the $(NH_4)_2H_1PMo_{12}O_{40}$(a) cluster (denoted as n = 2(a) in the figure). Dashed lines represent the best linear fits obtained via the least-squares method with the slopes shown in the figure; the errors reflect the standard error of the regression.

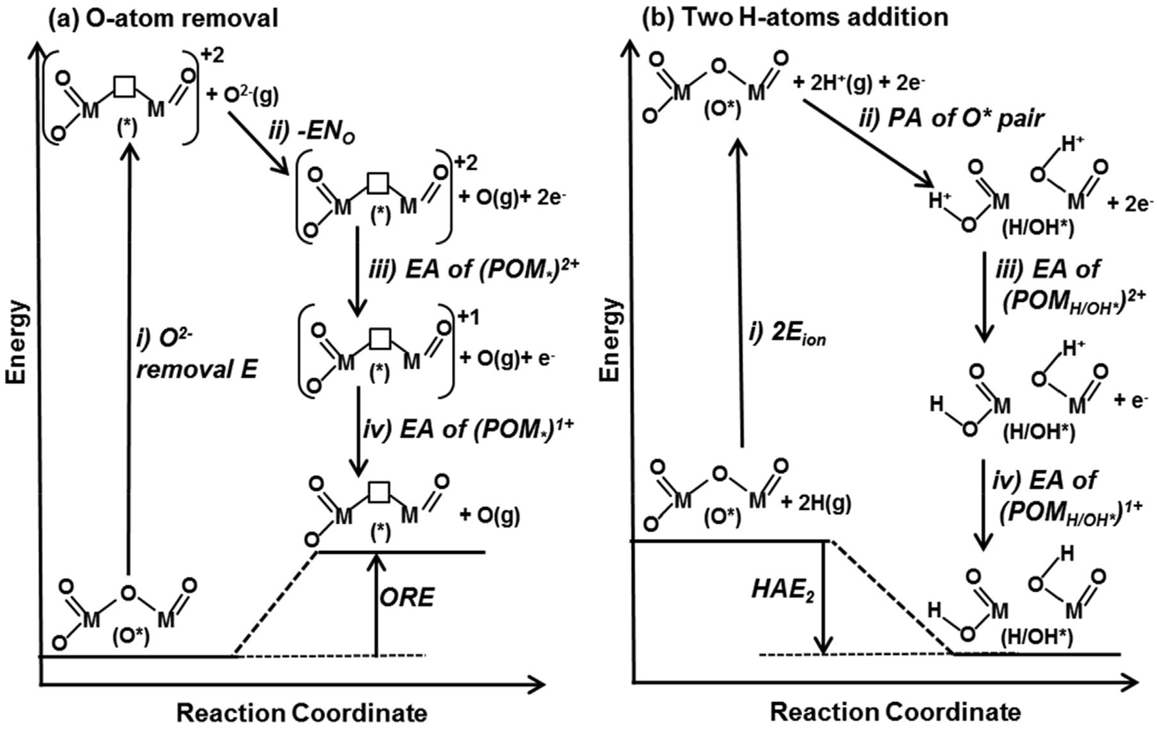

Scheme 5. A thermochemical cycle describing the energies associated with (a) the removal of an O-atom to form an O-vacancy (ORE; step ii; Scheme 4)[a] and (b) the addition of two H-atoms on an O-atom pair to form a OH pair ($HAE_1 + HAE_2$; steps iii and iv; Scheme 4)[b]. [a]O-atom removal energies equal the sum of energies for (i) the removal of $O^{2-}(g)$ from a neutral POM cluster to form an O-vacancy and a POM cluster with +2 charge ($(POM_*)^{2+}$); (ii) the removal of two electrons from $O^{2-}(g)$ to form an O(g) and two electrons ($-EN_o$), (iii) returning the first electron to the LUMO of the $(POM_*)^{2+}$ cluster (the electron affinity of $(POM_*)^{2+}$, EA); (iv) returning the second electron to the LUMO of one-electron reduced $(POM_*)^{1+}$ (EA of $(POM_*)^{1+}$) to form a neutral POM cluster with an O-vacancy. [b]Two H-atoms addition energies equal the sum of energies for (i) the ionization of two H(g) into two $H^+(g)$ and two electrons ($2E_{ion}$); (ii) the addition of two $H^+(g)$ on an O-atom pair to form a H/OH* center and a POM cluster with +2 charge ($(POM_{H/OH^*})^{2+}$) (the proton affinity of the O* pair; PA); (iii) returning the first electron to the LUMO of $(POM_{H/OH^*})^{2+}$ (EA of $(POM_{H/OH^*})^{2+}$); (iv) returning the second electron to the LUMO of one-electron reduced $(POM_{H/OH^*})^{1+}$ cluster (EA of $((POM_{H/OH^*})^{1+}$) to form a neutral POM cluster with a H/OH* center.

of an O(g) atom, -EN$_O$); (iii) returning the first electron to the lowest unoccupied molecular orbital (LUMO) of the $(POM_{*})^{2+}$ cluster (the electron affinity of the $(POM_{*})^{2+}$ cluster, EA); and (iv) returning the second electron to the LUMO of one-electron reduced $(POM_{*})^{1+}$ cluster (the electron affinity of the $(POM_{*})^{1+}$ cluster) to form a neutral POM cluster with an O-vacancy (Scheme 5a).

($HAE_1 + HAE_2$) values, in contrast, equal the sum of energies for (i) the ionization of two H(g) to form two H^+ and two electrons in the gas phase ($2E_{ion}$); (ii) the addition of these two protons on the designated O-atom pair to form a H/OH* center and a POM cluster with a 2+ charge ($(POM_{H/OH^*})^{2+}$) (the proton affinity of the O-atom pair, PA); (iii) placing the first electron at the LUMO of the $(POM_{H/OH^*})^{2+}$ cluster (the electron affinity of the $(POM_{H/OH^*})^{2+}$ cluster, EA); and (iv) placing the second electron at the LUMO of the one-electron reduced $(POM_{H/OH^*})^{1+}$ cluster (the electron affinity of the $(POM_{H/OH^*})^{1+}$ cluster) to form a neutral POM cluster with a H/OH* center (Scheme 5b).

For the range of O-atoms locations and POM compositions depicted in Fig. 1, O^{2-}-removal energies (step i; Scheme 5a) scale linearly with two H^+-addition energies (step ii in Scheme 5b) with a slope of 1.13 ± 0.08 (Fig. S.7; SI); the O-atoms at oxide surfaces with larger proton affinities (more negative two H^+-addition energies) require less energy to be removed as O^{2-} (smaller O^{2-}-removal energies). The O-atoms in the POM clusters with charge-balancing cations (NH_4^+) are more basic than the H^+-forms because of the higher electron density within NH_4^+-form of POM clusters; the proton affinity of the O* pair at O_1 location (step ii; Scheme 5b) becomes more negative from −1430 to −1508, to −1580, and to −1677 kJ mol^{-1} with increasing number of protons (n = 1, 2, 3) in $H_3PMo_{12}O_{40}$ replaced with NH_4^+ (Fig. S7; SI). Accordingly, the O^{2-} removal energy (step i; Scheme 5a) decreases from 2352 to 2258, to 2186, and to 2086 kJ mol^{-1} (Fig. S7; SI) because the electrostatic interaction energies between an O^{2-} anion and the +2 charged POM cluster with an O-vacancy are less negative for the POM clusters with higher electron density. The addenda atoms (Mo, Mo-V, W) and central atoms (Al^{3+}, P^{5+}) also influence the proton affinities and O^{2-} removal energies of the surface O-atoms through the charge-distributions within POM clusters; the O-atoms in Mo-based POM clusters are more basic and require smaller energies to be removed as O^{2-} than those with W-addenda atoms, while those in the POM clusters with Al^{3+} central atom are more basic and require smaller O^{2-} removal energies than with P^{5+} central atom (Fig. S.7; SI).

The ORE and ($HAE_1 + HAE_2$) values also depend on the first and second electron affinities of the +2 charged clusters with an O-vacancy or with two added protons, which are set by their LUMO energies (steps iii and iv in Schemes 5a and b). The LUMO of these POM clusters consist of d-orbitals at the addenda atoms, which are empty in their highest oxidation states (e.g. Mo^{6+}, W^{6+}, V^{5+}) [35]. Their energies thus depend on the identity and coordination of addenda atoms and on the identity of charge-balancing cations, all of which influence the POM electron density, but not on whether the +2 charged POM clusters contain an O-vacancy or two added protons. The LUMO energies of +2 charged POM clusters with an O-vacancy ($(POM_{*})^{2+}$; step iii in Scheme 5a) are nearly identical to those with two added protons ($(POM_{H/OH^*})^{2+}$; step iii in Scheme 5b) for each O-atom location in any given POM cluster (Fig. S.8a; SI) (−7.8 vs. −7.9, −7.4 vs. −7.4, and −7.3 vs. 7.3 eV for the +2 charged $H_3PMo_{12}O_{40}$, $H_3PW_{12}O_{40}$ and $(NH_4)_1H_2PMo_{12}O_{40}$ clusters containing an O-vacancy or two protons at O_1 location). These two LUMO energies vary in concert with O-atom location and POM composition with the slope of 0.97 ± 0.06 (Fig. S8a; SI) for the range of locations and POM compositions depicted in Fig. 1. The LUMO energies of one-electron reduced $(POM_{*})^{1+}$ and $(POM_{H/OH^*})^{1+}$ clusters (step iv in Schemes 5a and b) are also similar for each O-atom and scale linearly (slope = 0.95 ± 0.05; Fig. S.8b; SI). The LUMO energies of one electron-reduced POM clusters ($(POM_{*})^{1+}$ and $(POM_{H/OH^*})^{1+}$) for a given location and POM composition are, however, higher than those of the +2 charged POM clusters ($(POM_{*})^{2+}$ and $(POM_{H/OH^*})^{2+}$) because of the greater electron-electron repulsion in the more reduced oxide clusters (Fig. S.8a and S.8b; SI); the LUMO energy changes from −7.8 to −6.8, −7.4 to −6.4, and −7.3 to 6.3 eV upon one-electron reduction of the +2 charged $H_3PMo_{12}O_{40}$, $H_3PW_{12}O_{40}$ and $(NH_4)_1H_2PMo_{12}O_{40}$ POM clusters with a H/OH* center at O_1 location.

These analyses, in turn, show that the energies required for the removal of one O-atom (ORE) and the addition of two H-atoms ($HAE_1 + HAE_2$) are linearly related as a consequence of the relationship between the O^{2-}-removal and two H^+-addition energies (step i in Scheme 5a and step ii in Scheme 5b) and the first and second electron affinity of the +2 charged POM cluster with an O-vacancy and two protons (steps iii and iv in Scheme 5a and b). If O-atom removal and two H-addition processes sense the relevant LUMO energies to the same extent, ORE and ($HAE_1 + HAE_2$) values would scale linearly with a slope of unity and H_2O dissociation energies would be independent of any of these oxide properties (Eq. (14)). ($HAE_1 + HAE_2$) values, however, are less sensitive to LUMO energies than ORE values, because the covalent nature of O-H bonds in H/OH* leads to the placement of only a fraction of the two electrons brought by two H-atoms into the LUMO. Such covalency preserves a single-valued scaling between ORE and ($HAE_1 + HAE_2$) but with a slope slightly larger than unity (1.22 ± 0.04; Fig. 9a), leading to H_2O dissociation energies that depend on ORE and ($HAE_1 + HAE_2$) values (Eq. (14)). These two properties, ORE and ($HAE_1 + HAE_2$), are intercorrelated and thus can be used interchangeably as a complete descriptor of the oxide properties that determine H_2O dissociation energies and thus their reactivity in inner and outer sphere O_2 activation routes.

3.3.2. Intrinsic relations between first (HAE_1) and second (HAE_2) H-addition energies of oxide surfaces

In this section, we examine whether similar scaling relations would allow the interchangeable use of HAE_2 and HAE_1 as the relevant oxide properties. For a given O-atom pair, consisting an O-atom and the neighbor with the most favorable HAE, HAE_1 corresponds to the addition of the first H-atom at the O-atom in the pair with more negative HAE. HAE_2 corresponds to the addition of another H-atom at the remaining O-atom in the pair to form a vicinal OH pair. Once again, HAE_2 and HAE_1 increase in parallel (Fig. 9b) with a slope of 1.18 ± 0.09. Their linear scaling reflects their similar dependences on the properties of each O-atom location and POM composition, the nature of which is examined here using the thermochemical cycles depicted in Scheme 6.

HAE_1 reflects the energy change caused by the addition of a H-atom at the O-atom (O*) that exhibits more negative HAE between the two O-atoms in a pair. Scheme 6a shows a hypothetical cycle that includes: (i) the ionization of a H(g) to form a H^+ and an electron in the gas phase (E_{ion}); (ii) the addition of the proton at the designated O-atom on the oxide surface to form a +1 charged POM cluster with a OH* center ($(POM_{OH^*})^{+1}$; the proton affinity of the stoichiometric clusters; PA); and (iii) the return of an electron at the LUMO of $(POM_{OH^*})^{+1}$ (the electron affinity of $(POM_{OH^*})^{+1}$; EA) to form a neutral one-electron reduced POM cluster with a OH* center.

HAE_2 value reflects the energy change upon the addition of the second H-atom at the remaining O-atom in the pair to form a H/OH* center. HAE_2 values can be described by a thermochemical cycle (Scheme 6b), which includes: (i) E_{ion}, (ii) the addition of H^+ at the O-atom vicinal to the OH* center (formed upon the first H-addition) to form a one-electron reduced POM cluster with two added protons ($(POM_{H/OH^*})^{+1}$; proton affinity; PA); and (iii) the return of an electron to the LUMO of the one-electron reduced

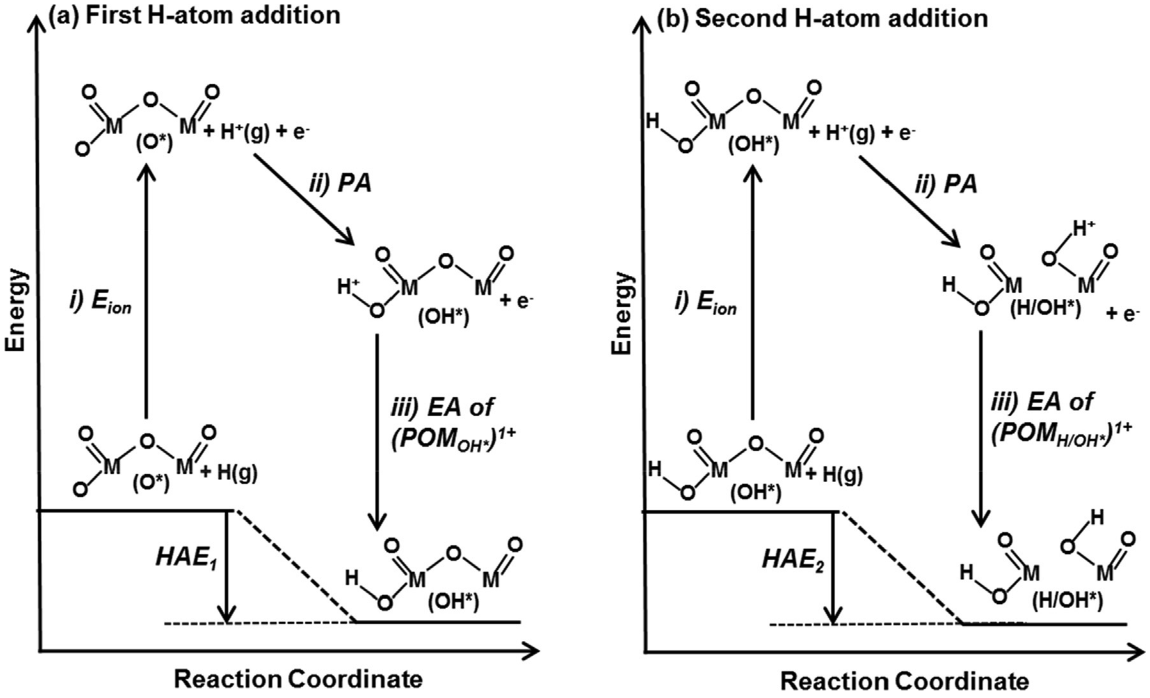

Scheme 6. A thermochemical cycle describing the energies associated with (a) the first and (b) the second H-atom addition on an O-atom pair (HAE_1 and HAE_2; steps iii and iv; Scheme 4)[a,b]. [a]HAE_1 reflects combined energies for (i) the ionization of a H(g) into a H^+(g) and an electron (E_{ion}); (ii) the addition of a H^+(g) on a designated O-atom in a O-atom pair (the proton affinity; PA) to form a +1 charged POM cluster with a OH^* center ($(POM_{OH^*})^{1+}$); (iii) returning an electron to the LUMO of $(POM_{OH^*})^{1+}$ (EA of $(POM_{OH^*})^{1+}$) to form a neutral POM cluster with a OH^* center. [b]HAE_2 reflects combined energies for (i) E_{ion} (ii) the addition of a H^+(g) on the remaining O-atom in a pair (PA) to form an one-electron reduced POM cluster with two added protons ($(POM_{H/OH^*})^{1+}$); (iii) returning an electron to the LUMO of $(POM_{H/OH^*})^{1+}$ (EA of $(POM_{H/OH^*})^{1+}$) to form a neutral POM cluster with a H/OH^* center.

$(POM_{H/OH^*})^{+1}$ cluster (the electron affinity of the $(POM_{H/OH^*})^{+1}$ cluster; EA) to form a neutral two-electron reduced cluster with a H/OH^* center.

The proton affinity (PA) of the O-atom at which the first proton is added (step ii; Scheme 6a) ranges between −963 to −807 kJ mol^{-1} (Fig. S9a; SI), depending on the O-atom location and the POM composition. The presence of charge-balancing cations breaks the symmetry within the POM cluster and causes a slight deviation in the proton affinities of O-atoms in a given cluster, depending on their locations; PA ranges between −860 and −841 kJ mol^{-1} for O_1–O_4 location in a $H_3PMo_{12}O_{40}$ cluster. These deviations among O-atom locations, however, are minor compared with the changes in PA with varying POM composition. The proton affinity of the O_1-atom becomes increasingly more negative from −846 to −879, to −917, and to −963 kJ mol^{-1} as one, two, and three H^+ in $H_3PMo_{12}O_{40}$ are substituted with NH_4^+ (Fig. S.9a; SI), because of the increase in the electron density within the cluster upon such replacements. Accordingly, the PA of the vicinal O-atoms at which the second proton is added (with the first H-atom already added; step ii; Scheme 6b) also becomes more negative (from −859 to −895, to −923, and to −963 kJ mol^{-1} for $(NH_4)_1H_2PMo_{12}O_{40}$, $(NH_4)_2H_1PMo_{12}O_{40}$(a), and $(NH_4)_3PMo_{12}O_{40}$ clusters; Fig. S.9a; SI). The O-atoms in the POM clusters with W-addenda atoms are slightly less basic than those with Mo-atoms, and similarly, the vicinal O-atoms (with the first H-atom already added) are also less basic to a similar extent; the PA of O_1-atom in $H_3PW_{12}O_{40}$ is less negative than that in $H_3PMo_{12}O_{40}$ (−807 vs. 846 kJ mol^{-1}; Fig. S.9a; SI) and so does the vicinal O-atom at which the second proton is added (with the first H-atom already added) (−831 vs. −860 kJ mol^{-1}; Fig. S.9a; SI). These trends show that the POM composition influences the basicity of the two O-atoms in the pair to the similar extent and that the PA of the O-atom at which the first proton is added (step ii; Scheme 6a) varies linearly with that of the vicinal O-atom at which the second proton is added (with the first H-atom already added; step ii; Scheme 6b); the slope of this relationship is unity (1.0 ± 0.1; Fig. S9a; SI) for the range of O-atoms and POM compositions examined.

HAE_1 and HAE_2 values also depend on the electron affinities of $(POM_{OH^*})^{+1}$ and $(POM_{H/OH^*})^{+1}$ clusters (steps iii; Schemes 6a and b), which are set by their LUMO energies. These two LUMO energies, again, vary in parallel with O-atom locations and POM compositions; the slope of this linear relationship is 1.08 ± 0.07 (Fig. S9b; SI). The LUMO energies of the one-electron reduced $(POM_{H/OH^*})^{+1}$ clusters are, in fact, very similar to those of $(POM_{OH^*})^{+1}$ clusters at each O-atom location and POM composition; the LUMO energies of $(POM_{OH^*})^{+1}$ and one-electron reduced $(POM_{H/OH^*})^{+1}$ clusters are −6.8 vs. −6.8, −6.4 vs. −6.4, and −6.4 vs. −6.3 eV for $H_3PMo_{12}O_{40}$, $H_3PW_{12}O_{40}$ and $(NH_4)_1H_2PMo_{12}O_{40}$ POM clusters, respectively, with one or two protons added at a given O_1 location. Such trends are consistent with the covalent nature of the O-H bonds that are formed upon the first H-atom addition, because otherwise the LUMO energies of the one-electron reduced $(POM_{H/OH^*})^{+1}$ clusters would be much less negative than those of $(POM_{OH^*})^{+1}$ clusters due to the greater electron-electron repulsions.

These analyses show that HAE_2 values scale linearly with HAE_1 (the slope = 1.18 ± 0.09; Fig. 9b) because of the proton affinities of the two O-atoms in the pair (step ii in Schemes 6a and b) and the electron affinities of $(POM_{OH^*})^{+1}$ and $(POM_{H/OH^*})^{+1}$ clusters (step iii in Schemes 6a and b) that vary in parallel with O-atom locations and POM compositions. Such a linear correlation, in turn, allows the interchangeable use of these oxide properties (HAE_1, HAE_2) in describing the H_2O dissociation energies on O-vacancies (ΔE_{H_2O}; Eq. (14)).

3.3.3. Intrinsic relations between H_2O dissociation energy on O-vacancies (ΔE_{H_2O}) and the second H-addition energies (HAE_2)

The intrinsic relations between ORE and ($HAE_1 + HAE_2$) values (Fig. 9a) and between HAE_1 and HAE_2 values (Fig. 9b) indicate that any effects of these oxide properties on H_2O dissociation energies (ΔE_{H_2O}; Eq. (14)) can be fully described by any one of these energies. The description of the barriers of the outer sphere O_2 activation routes ($\Delta E_{out,1}{}^{TS}$; step 3 in Scheme 1) in terms of ($E_{int}{}^{0}$-HAE$_2$) descriptor (Eq. (13); Section 3.2) makes it convenient to examine HAE$_2$ as the complete oxide descriptor of H_2O dissociation energies on O-vacancies.

Fig. 10 shows the linear trend between H_2O dissociation energies (ΔE_{H_2O}) and HAE$_2$ (slope = −0.38 ± 0.09) for all O-atom locations and POM compositions examined. This trend is consistent with the form of Eq. (14), derived from the thermochemical cycle in Scheme 4, and with the interrelated character of HAE$_1$, HAE$_2$, and ORE (Fig. 9). These results, in turn, show that HAE$_2$ indeed serves as a complete descriptor of the thermodynamics of H_2O dissociation on O-vacancies to form H/OH* species.

3.4. Oxide properties that account for the relative rates of inner and outer sphere O_2 activation routes

The relative contributions of inner and outer sphere O_2 activation routes (r_{in}/r_{out}; χ; Eq. (7)) depend sensitively on the prevalent concentration of H_2O formed during oxidation catalysis because the reactant states of these two O_2 activation pathways, O-vacancies (*) and vicinal OH pairs (H/OH*), are typically in quasi-equilibrium via H_2O dissociation (step 2; Scheme 1). Higher H_2O contents favor outer sphere routes by capping O-vacancies to form H/OH* centers, the reactant state of the outer sphere routes [4]. Inner sphere routes, in contrast, become prevalent at higher temperatures because the very negative H_2O dissociation enthalpies render outer sphere routes to be enthalpically more favorable than inner sphere routes [4]. Specific oxide properties also influence the inner and outer sphere selectivities (χ; Eq. (7)) in a manner that we explore here by combining the catalytic descriptors for each elementary step (Scheme 1) derived in Sections 3.1–3.3.

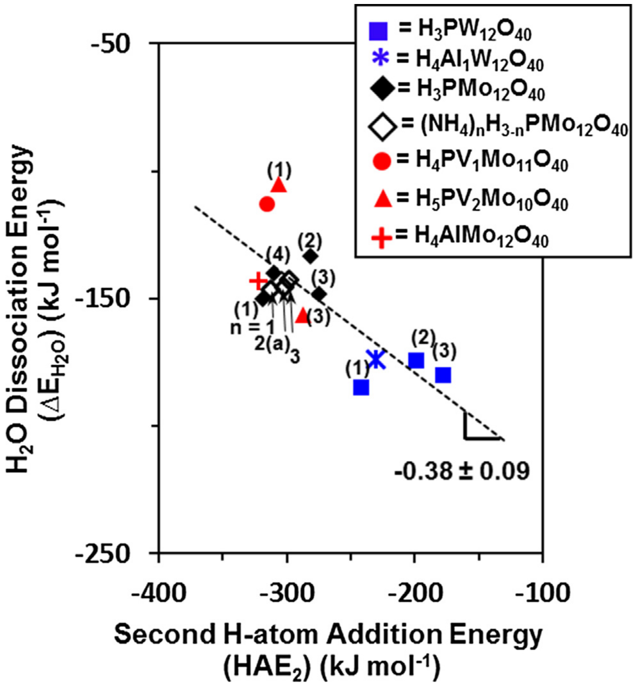

Fig. 10. DFT-derived H_2O dissociation energy on O-vacancies to form OH pairs (ΔE_{H_2O}; step 2; Scheme 1) as a function of the second H-atom addition energies (HAE$_2$; step iv; Scheme 4). The POM compositions and the corresponding symbols are shown in the legend. These values are calculated at O-vacancies formed at O_1 location (in Fig. 1), except for $H_3PW_{12}O_{40}$ (■), $H_3PMo_{12}O_{40}$ (◆), and $H_5PV_2Mo_{10}O_{40}$ (▲) clusters, for which O-vacancy locations are shown inside the parenthesis close to each data point. The numbers of NH_4^+ (n = 1,2,3) in $(NH_4)_nH_{3-n}PMo_{12}O_{40}$ clusters are shown next to the corresponding data; two protons vicinal to the O_1-atom are substituted with NH_4^+ in the $(NH_4)_2H_1PMo_{12}O_{40}$(a) cluster (denoted as n = 2(a) in the figure). The dashed line represents the best linear fit via the least-squares method with the slope shown in the figure; the error reflects the standard error of the regression.

The descriptions of inner and outer sphere activation barriers ($\Delta E_{in}{}^{TS}$ and $\Delta E_{out,1}{}^{TS}$) and H_2O dissociation energies (ΔE_{H_2O}) in terms of HAE$_2$ (and $E_{int}{}^{0}$ for outer sphere routes) show that these oxide properties determine the relative rates of inner and outer sphere pathways (χ) via Eq. (7). Inner sphere routes (step 1; Scheme 1) are mediated by very early transition states (TS$_{in}$) on redox-active oxides; consequently, the formation energy of this TS$_{in}$ from an O-vacancy and an O_2(g) molecule ($\Delta E_{in}{}^{TS}$) is insensitive to the identity or properties of the O-atom that is removed to form the vacancy (Section 3.1). Outer sphere O_2 activation rates (step 3; Scheme 1) depend on the stability of TS$_{out,1}$ that mediates the transfer of one of the H-atoms from H/OH* to O_2 to form the ·OOH intermediate. The energy of formation of this TS$_{out,1}$ from H/OH* and O_2(g) precursors ($\Delta E_{out,1}{}^{TS}$) scales with the value of ($E_{int}{}^{0}$-HAE$_2$) (Eq. (13); Section 3.2). $E_{int}{}^{0}$ values, which reflect the ·OOH-surface interaction energies at the product state of the first H-atom transfer, are similar for all H/OH* centers at different locations in compositionally-diverse POM clusters, except for those near large interacting cations (Fig. 8; Section 3.2.2). Consequently, HAE$_2$, which reflects the energy required to cleave the weaker O-H bond in H/OH*, acts as a single and complete descriptor of the outer sphere O_2 activation rates (Fig. 7a) for all H/OH* centers that are non-vicinal to large-charge balancing cations. In the latter case, the interactions between the ·OOH intermediate and the large vicinal cation become specific to their distances and to the chemical identity and size of the cations and thus requires explicit DFT-derived value of $E_{int}{}^{0}$ for the accurate description of outer sphere routes (Fig. 7b), because such interactions stabilize ·OOH species and lead to more negative $E_{int}{}^{0}$ (Fig. 8) and to lower $\Delta E_{out,1}{}^{TS}$ values. The equilibrium between * and H/OH*, the reactants along with O_2(g) in inner and outer sphere routes, depends on the H_2O dissociation energy on * (ΔE_{H_2O}), which can also be described by HAE$_2$ (Fig. 10). As a result, HAE$_2$ is sufficient to describe the values of χ (Eq. (7)) for each location and POM composition, as long as large interacting cations are not present at vicinal locations.

Inner and outer sphere rate ratios (r_{in}/r_{out}; χ; Eq. (7)) calculated at each location in diverse POM clusters are shown in Fig. 11 as a function of HAE$_2$; these χ values are calculated at 0.01 bar H_2O, the atypical H_2O pressure during oxidation catalysis. Free energies of inner and outer sphere transition states ($G_{in}{}^{TS}$ and $G_{out}{}^{TS}$), which determine the rate ratios (χ) via Eq. (7), include different enthalpic and entropic components and thus must be rigorously assessed in order to accurately estimate the O_2 activation selectivities. These $G_{in}{}^{TS}$and $G_{out}{}^{TS}$ values and the free energy of H_2O molecules (G_{H_2O}) are estimated at 453 K and standard O_2 and H_2O pressures (1 bar) using Eqs. (1) and (2) and DFT-derived electronic energies ($E_{in}{}^{TS}$ and $E_{out,1}{}^{TS}$in Figs. 3 and 7) and zero-point vibrational energies and thermal contributions of enthalpies and entropies calculated via the statistical mechanical formalism (details in Section 2).

The trends in Fig. 11 show that HAE$_2$ indeed functions as a complete descriptor of the rate ratios (r_{in}/r_{out}; χ). The O-atoms at oxide surfaces with less negative HAE$_2$ favor outer sphere routes over inner sphere pathways, as shown by the (r_{in}/r_{out}) rate ratio estimated at O_1-location in the $H_3PW_{12}O_{40}$ POM cluster that is much less then unity (6×10^{-10} at 453 K; 0.01 bar H_2O; Fig. 11). This prediction is in line with the lack of incorporation of ^{17}O-atoms into W-O-W bonds during exposure of aqueous $[PW_{12}O_{40}]^{3-}$ anions reduced electrochemically to $^{17}O_2$ molecules and with the exclusive presence of ^{17}O-atoms in H_2O_2 and H_2O [8]. The O-atoms at

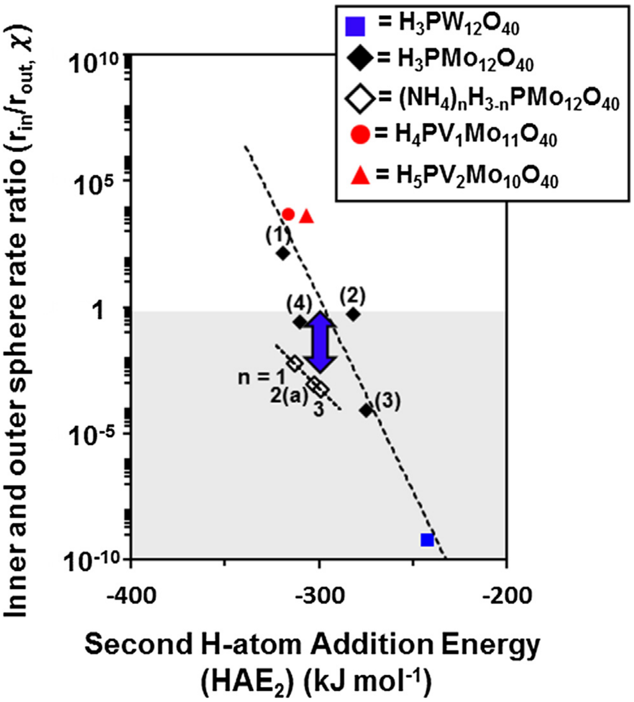

Fig. 11. DFT-derived inner and outer sphere rate ratios (χ; 453 K; 0.01 bar H_2O; Eq. (7)) as a function of second H-atom addition energies (HAE_2). The POM compositions and the corresponding symbols are shown in the legend. These calculations involve O_1-atoms (in Fig. 1), except for the $H_3PMo_{12}O_{40}$ cluster (◆), for which O-atom locations are shown inside the parenthesis close to each data point. The numbers of NH_4^+ (n = 1,2,3) in $(NH_4)_nH_{3-n}PMo_{12}O_{40}$ clusters are shown next to the corresponding data. Two protons vicinal the O_1 location are substituted with NH_4^+ in the $(NH_4)_2H_1PMo_{12}O_{40}$(a) cluster (denoted as n = 2(a); Fig. 1). The shaded region reflects the χ values less than unity, preferring the outer sphere routes. Dashed lines represent the best fits to the exponential function.

O_1-location in $H_4PV_1Mo_{11}O_{40}$ and $H_5PV_2Mo_{10}O_{40}$ clusters, in contrast, exhibit much more negative HAE_2 values (-316 and -307 kJ mol^{-1}, respectively) than that in $H_3PW_{12}O_{40}$ (-242 kJ mol^{-1}) and thus would prefer inner sphere routes ($\chi = 4.5 \times 10^3$ and 4.2×10^3; Fig. 11; 453 K; 0.01 bar H_2O). Such predictions are consistent with the incorporation of ^{17}O-atoms into the framework of $[PV_2Mo_{10}O_{40}]^{5-}$ anions upon reactions of $^{17}O_2(g)$ with O-vacancies formed in such anions via electrochemical methods [8].

Large charge-balancing cations (e.g., NH_4^+) interact with ·OOH intermediate that are involved in the first H-atom transfer step in the outer sphere routes (step 3; Scheme 1). Such additional stabilization by large vicinal cations leads to much negative $E_{int}{}^0$ (Fig. 8) for ·OOH species formed at H/OH* centers located near such cations and to lower $\Delta E_{out,1}{}^{TS}$ values. Consequently, O-atoms near NH_4^+ (at O_1-location in $(NH_4)_1H_2PMo_{12}O_{40}$, $(NH_4)_2H_1PMo_{12}O_{40}$(a), and $(NH_4)_3PMo_{12}O_{40}$ clusters; denoted as n = 1, 2a, 3 in Fig. 11) show a stronger preference for the outer sphere routes than expectations from their HAE_2 values and the trend observed on other O-atoms and POM compositions. Such effects of charge-balancing cations, in fact, allow flexibility of modifying oxide surfaces to favor the outer sphere O_2 activation routes and to circumvent the involvements of the electrophilic bound OO* species during re-oxidation events. These cation effects depend on their size, charge, and distance from ·OOH intermediates; detailed assessments on the effects of cation identities on the O_2 activation rates and selectivities are beyond the scope of the present study, but may be useful to find optimal cations to achieve desired selectivities.

The analyses presented here have used POM clusters as illustrative oxides because of their advantages in performing systematic computational assessments, but the conclusions derived are applicable to other practical oxides with octahedral coordination. The O-atoms at oxide surfaces with more negative HAE_2 values exhibit a greater preference for the inner sphere routes (Fig. 11). HAE_2 scales linearly with HAE_1 (Fig. 9b), the oxide property that was previously identified as an accurate descriptor for H-abstraction abilities of nucleophilic O-atoms at oxide surfaces and thus for their reactivities in ODH reactions [21,26]. These results, in turn, predict that at a given condition (e.g., temperature and H_2O contents), O-atoms that are more reactive in ODH reactions (more negative HAE_1 and HAE_2) are more likely to form bound OO* intermediates via inner sphere routes during the re-oxidation steps. The charge-balancing cations can be selected to alter their propensity to either inner or outer sphere routes by modifying the ·OOH-surface interaction energies ($E_{int}{}^0$) that influence outer sphere rates. These predictions of O_2 activation selectivities provide the design strategies for oxide systems that are selective for inner or outer sphere routes with their significant consequences for reactivity and selectivity of O_2-derived species in oxidation catalysis.

4. Conclusions

The dynamics and thermodynamics of inner and outer sphere O_2 activation routes are theoretically assessed at different O-atoms in POM clusters with a wide range of chemical compositions. Inner sphere routes form bound peroxo (OO*) species by activating $O_2(g)$ on O-vacancies (*) (step 1; Scheme 1). The transition states (TS_{in}) that mediate these routes occur very early along the O_2 activation reaction coordinate, and thus, their formation energies from * and $O_2(g)$ precursors ($\Delta E_{in}{}^{TS}$) are insensitive to the oxide compositions and to the locations of O-atoms that are removed to form O-vacancies.

Outer sphere routes form $H_2O_2(g)$ through an activation of $O_2(g)$ on H/OH* centers (step 3; Scheme 1) that are formed via H_2O dissociation on O-vacancies (step 2; Scheme 1). The transition states ($TS_{out,1}$) that mediate the first H-atom transfer from H/OH* to $O_2(g)$ determine the outer sphere O_2 activation rates. The formation energy of this $TS_{out,1}$ from H/OH* and $O_2(g)$ precursors (and thus $\Delta E_{out,1}{}^{TS}$ barrier) is a single-valued function of ($E_{int}{}^0$-HAE_2). The $E_{int}{}^0$ values reflect the ·OOH-surface interaction energies at the product state of the first H-atom transfer step and are similar for all H/OH* centers at different O-atom locations in POM clusters, as long as they do not involve large interacting cations. Consequently, HAE_2, which reflects the energy required to cleave the weaker O-H bond of the H/OH* center, acts as a complete descriptor for $\Delta E_{out,1}{}^{TS}$ for all H/OH* centers that are non-vicinal to large charge-balancing cations. In the latter case, the interactions between the ·OOH intermediate and the large vicinal cation depend on their distance and the chemical identity and size of the cations and must be explicitly calculated, because such interactions lead to more negative $E_{int}{}^0$ and to lower $\Delta E_{out,1}{}^{TS}$ values. H_2O dissociation energies on O-vacancies (ΔE_{H_2O}; step 3; Scheme 1), which determine the equilibrium between the two types of two-electron reduced centers (* and H/OH*), also behave as a single-valued function of HAE_2.

These trends, in turn, give HAE_2 as a complete catalytic descriptor of the O_2 activation selectivity (r_{in}/r_{out}; χ) for all H/OH* centers non-vicinal to large charge-balancing cations. The O-atoms at oxide surfaces with more negative HAE_2 values favor inner sphere routes over outer sphere pathways. HAE_2 scales linearly with HAE_1, the oxide property that reflects H-abstraction abilities of nucleophilic O-atoms. These results predict that more reactive O-atoms in ODH reactions (more negative HAE_1 and HAE_2) are more likely to form bound OO* species during the re-oxidation steps. Large charge-balancing cations locally modify ·OOH-surface interaction energies ($E_{int}{}^0$) that determine outer sphere rates, thereby altering the propensity of O-atoms to inner or outer sphere routes.

The surface-bound OO* intermediates involved in inner sphere routes are electrophilic in nature; their formation in the re-oxidation steps, thus, significantly impacts the reactivity and selectivity of oxides in oxidation catalysis. Through detailed assessments of the oxide properties that influence the O_2 activation rates and selectivities, this work provides the design strategies for the oxide systems that are selective towards either inner or outer sphere routes during Mars-van Krevelen redox cycles. More importantly, the analytic framework demonstrated in this work provides a general formalism that can be used to identify more accurate catalytic descriptors for rates and selectivities of many other reactions.

Acknowledgements

The authors thank Drs. Robert Carr, Randall Meyer, and Lucas Koziol for their technical discussions and careful proofreading of the manuscript. We also thank Ari Fischer, Haefa Mansour and Drs. Jiahan Xie and Shashikant Kadam at the University of California at Berkeley for their help in proofreading the manuscript. This work has been supported by the U.S. Department of Energy (DOE), Office of Science, Office of Basic Energy Sciences (Contract No. DE-AC05-76RL0-1830) and by a research contract between ExxonMobil Research and Engineering Co. and the University of California at Berkeley. A portion of the research was performed using EMSL facilities (the project number of 48772), a DOE Office of Science User Facility sponsored by the Office of Biological and Environmental Research. This work also used the computational resources at the National Energy Research Scientific Computing Center (NERSC), a U.S. Department of Energy Office of Science User Facility operated under Contract No. DE-AC02-05CH1123 and at the Extreme Science and Engineering Discovery Environment (XSEDE) [49], supported by National Science Foundation (grant number ACI-1548562).

Appendix A. Supplementary material

Supplementary data to this article can be found online at https://doi.org/10.1016/j.jcat.2019.07.048.

References

[1] P. Mars, D.W. Van Krevelen, Oxidations carried out by means of vanadium oxide catalysts, Chem. Eng. Sci. 3 (1954) 41–59, https://doi.org/10.1016/S0009-2509(54)80005-4.

[2] C. Zhao, I.E. Wachs, An Operando Raman, IR, and TPSR spectroscopic investigation of the selective oxidation of propylene to acrolein over a model supported vanadium oxide monolayer catalyst, J. Phys. Chem. C. 112 (2008) 11363–11372, https://doi.org/10.1021/jp801562g.

[3] A. Goodrow, A.T. Bell, A theoretical investigation of the selective oxidation of methanol to formaldehyde on isolated vanadate species supported on silica, J. Phys. Chem. C. 111 (2007) 14753–14761, https://doi.org/10.1021/jp072627a.

[4] S. Kwon, P. Deshlahra, E. Iglesia, Dioxygen activation routes in Mars-van Krevelen redox cycles catalyzed by metal oxides, J. Catal. 364 (2018) 228–247, https://doi.org/10.1016/j.jcat.2018.05.016.

[5] X. Rozanska, E. Kondratenko, J. Sauer, Oxidative dehydrogenation of propane: differences between N_2O and O_2 in the reoxidation of reduced vanadia sites and consequences for selectivity, J. Catal. 256 (2008) 84–94, https://doi.org/10.1016/j.jcat.2008.03.002.

[6] N. Mizuno, H. Weiner, R.G. Finke, Co-oxidative epoxidation of cyclohexene with molecular oxygen, isobutyraldehyde reductant, and the polyoxoanion-supported catalyst precursor [(n-C4H9)(4)N](5)Na-3[(1,5-COD)IrP2W15Nb3O62], J. Mol. Catal. A Chem. 114 (1996) 15–28, https://doi.org/10.1016/S1381-1169(96)00301-9.

[7] R. Neumann, M. Levin, Aerobic oxidative dehydrogenations catalyzed by the mixed-addenda heteropolyanion PV2Molo0405: a kinetic and mechanistic study, J. Am. Chem. Soc. 114 (1992) 7278–7286, https://doi.org/10.1021/ja00044a044.

[8] D.C. Duncan, C.L. Hill, Mechanism of reaction of reduced polyoxometalates with O_2 evaluated by $_{17}O$ NMR, J. Am. Chem. Soc. 119 (1997) 243–244, https://doi.org/10.1021/ja9627860.

[9] D.C. Ashley, D.W. Brinkley, J.P. Roth, Oxygen isotope effects as structural and mechanistic probes in inorganic oxidation chemistry, Inorg. Chem. 49 (2010) 3661–3675, https://doi.org/10.1021/ic901778g.

[10] D.A. Kopp, S.J. Lippard, Soluble methane monooxygenase: activation of dioxygen and methane, Curr. Opin. Chem. Biol. 6 (2002) 568–576, https://doi.org/10.1016/S1367-5931(02)00366-6.

[11] G.J. Hutchings, Methane activation by selective oxidation, Top. Catal. 59 (2016) 658–662, https://doi.org/10.1007/s11244-016-0542-x.

[12] M. Ravi, M. Ranocchiari, J.A. van Bokhoven, A critical assessment of the direct catalytic oxidation of methane to methanol, Angew. Chemie Int. Ed. 56 (2017) 16464–16483, https://doi.org/10.1002/anie.201702550.

[13] P.P. Chen, P. Nagababu, S.S. Yu, S.I. Chan, Development of the tricopper cluster as a catalyst for the efficient conversion of methane into MeOH, Chem. Commun. 6 (2014) 429–437, https://doi.org/10.1002/cctc.201300473.

[14] C. Hammond, M.M. Forde, M. Hasbi, A. Rahim, A. Thetford, Q. He, et al., Direct catalytic conversion of methane to methanol in an aqueous medium by using copper-promoted Fe-ZSM-5, Angew. Chem. Int. Ed. Engl. 51 (2012) 5129–5133, https://doi.org/10.1002/anie.201108706.

[15] H. Feng, J.W. Elam, J.A. Libera, M.J. Pellin, P.C. Stair, Oxidative dehydrogenation of cyclohexane over alumina-supported vanadium oxide nanoliths, J. Catal. 269 (2010) 421–431, https://doi.org/10.1016/j.jcat.2009.11.026.

[16] Z. Skoufa, E. Heracleous, a.a. Lemonidou, On ethane ODH mechanism and nature of active sites over NiO-based catalysts via isotopic labeling and methanol sorption studies, J. Catal. 322 (2015) 118–129. doi: 10.1016/j.jcat.2014.11.014.

[17] M.D. Argyle, K. Chen, C. Resini, C. Krebs, A.T. Bell, E. Iglesia, Extent of reduction of vanadium oxides during catalytic oxidation of alkanes measured by in-situ UV−Visible spectroscopy, J. Phys. Chem. B. 108 (2004) 2345–2353, https://doi.org/10.1021/jp030989m.

[18] K. Chen, E. Iglesia, A.T. Bell, Isotopic tracer studies of reaction pathways for propane oxidative dehydrogenation on molybdenum oxide catalysts, J. Phys. Chem. B. 105 (2001) 646–653, https://doi.org/10.1021/jp002100x.

[19] L. Annamalai, Y. Liu, S. Ezenwa, Y. Dang, S.L. Suib, P. Deshlahra, Influence of tight confinement on selective oxidative dehydrogenation of ethane on MoVTeNb mixed oxides, ACS Catal. 8 (2018) 7051–7067, https://doi.org/10.1021/acscatal.8b01586.

[20] H. Liu, E. Iglesia, Selective oxidation of methanol and ethanol on supported ruthenium oxide clusters at low temperatures, J. Phys. Chem. B. 109 (2005) 2155–2163, https://doi.org/10.1021/jp0401980.

[21] P. Deshlahra, E. Iglesia, Methanol oxidative dehydrogenation on oxide catalysts: molecular and dissociative routes and hydrogen addition energies as descriptors of reactivity, J. Phys. Chem. C. 118 (2014) 26115–26129, https://doi.org/10.1021/jp507922u.

[22] M.D. Argyle, K. Chen, E. Iglesia, A.T. Bell, In situ UV-visible spectroscopic measurements of kinetic parameters and active sites for catalytic oxidation of alkanes on vanadium oxides, J. Phys. Chem. B. 109 (2005) 2414–2420, https://doi.org/10.1021/jp040166c.

[23] R. Prabhakar, K. Morokuma, C.L. Hill, D.G. Musaev, Insights into the mechanism of selective olefin epoxidation catalyzed by [gamma-(SiO4)W10O32H4]4. A computational study, Inorg. Chem. 45 (2006) 5703–5709, https://doi.org/10.1021/ic060725p.

[24] R. Neumann, M. Dahan, A ruthenium-substituted polyoxometalate as an inorganic dioxygenase for activation of molecular oxygen, Nature 388 (1997) 353–355, https://doi.org/10.1038/41039.

[25] N. Mizuno, K. Kamata, Catalytic oxidation of hydrocarbons with hydrogen peroxide by vanadium-based polyoxometalates, Coord. Chem. Rev. 255 (2011) 2358–2370, https://doi.org/10.1016/j.ccr.2011.01.041.

[26] P. Deshlahra, E. Iglesia, Reactivity and selectivity descriptors for the activation of C-H bonds in hydrocarbons and oxygenates on metal oxides, J. Phys. Chem. C. 120 (2016) 16741–16760, https://doi.org/10.1021/acs.jpcc.6b04604.

[27] G. Kresse, J. Hafner, Ab initio molecular-dynamics simulation of liquid-metal-amorphous-semiconductor transition in germanium, Phys. Rev. B. 49 (1994) 14251–14269.

[28] G. Kresse, J. Furthmüller, Efficient iterative schemes for ab initio total-energy calculations using a plane-wave basis set, Phys. Rev. B 54 (1996) 11169–11186. http://www.ncbi.nlm.nih.gov/pubmed/9984901.

[29] G. Kresse, J. Furthmüller, Efficiency of ab-initio total energy calculations for metals and semiconductors using a plane-wave basis set, Comput. Mater. Sci. 6 (1996) 15–50.

[30] J.P. Perdew, J.A. Chevary, S.H. Vosko, K.A. Jackson, M.R. Pederson, D.J. Singh, et al., Atoms, molecules, solids, and surfaces: applications of the generalized gradient approximation for exchange and correlation, Phys. Rev. B. 46 (1992) 6671–6687, https://doi.org/10.1103/PhysRevB.48.4978.2.

[31] P.E. Blöchl, Projector augmented-wave method, Phys. Rev. B. 50 (1994) 17953–17979.

[32] G. Kresse, D. Joubert, From ultrasoft pseudopotentials to the projector augmented-wave method, Phys. Rev. B. 59 (1999) 1758–1775.

[33] H.J. Monkhorst, J.D. Pack, Special points for Brillouin-zone integrations, Phys. Rev. B. 13 (1976) 5188–5192.

[34] G. Makov, M.C. Payne, Periodic boundary conditions in ab initio calculations, Phys. Rev. B. 51 (1995) 4014–4022, https://doi.org/10.1103/PhysRevB.51.4014.
[35] P. Deshlahra, R.T. Carr, S.-H. Chai, E. Iglesia, Mechanistic details and reactivity descriptors in oxidation and acid catalysis of methanol, ACS Catal. 5 (2015) 666–682, https://doi.org/10.1021/cs501599y.
[36] D. Schröder, S. Shaik, H. Schwarz, Two-state reactivity as a new concept in organometallic chemistry, Acc. Chem. Res. 33 (2000) 139–145, https://doi.org/10.1021/ar990028j.
[37] S. Shaik, D. Danovich, A. Fiedler, D. Schröder, H. Schwarz, Two-state reactivity in organometallic gas-phase ion chemistry, Helv. Chim. Acta. 78 (1995) 1393–1407, https://doi.org/10.1002/hlca.19950780602.
[38] A.B. Getsoian, V. Shapovalov, A.T. Bell, DFT + U investigation of propene oxidation over bismuth molybdate: active sites, reaction intermediates, and the role of bismuth, J. Phys. Chem. C. 117 (2013) 7123–7137, https://doi.org/10.1021/jp400440p.
[39] G. Henkelman, B.P. Uberuaga, H. Jonsson, A climbing image nudged elastic band method for finding saddle points and minimum energy paths, J. Chem. Phys. 113 (2000) 9901–9904.
[40] G. Henkelman, H. Jónsson, A dimer method for finding saddle points on high dimensional potential surfaces using only first derivatives, J. Chem. Phys. 111 (1999) 7010–7022, https://doi.org/10.1063/1.480097.
[41] Donald A. McQuarrie, Statistical Mechanics, University Science Books, Sausalito, CA, 2000.
[42] C.T. Campbell, J.R.V. Sellers, Enthalpies and entropies of adsorption on well-defined oxide surfaces: experimental measurements, Chem. Rev. 113 (2013) 4106–4135, https://doi.org/10.1021/cr300329s.
[43] S.L. Dudarev, D.N. Manh, A.P. Sutton, Effect of Mott-Hubbard correlations on the electronic structure and structural stability of uranium dioxide, Philos. Mag. Part B. 75 (1997) 613–628, https://doi.org/10.1080/13642819708202343.
[44] S.L. Dudarev, G.A. Botton, S.Y. Savrasov, C.J. Humphreys, A.P. Sutton, Electron-energy-loss spectra and the structural stability of nickel oxide: an LSDA+U study, Phys. Rev. B. 57 (1998) 1505–1509.
[45] S. Lutfalla, V. Shapovalov, A.T. Bell, Calibration of the DFT/GGA+U method for determination of reduction energies for transition and rare earth metal oxides of Ti, V, Mo, and Ce, J. Chem. Theory Comput. 7 (2011) 2218–2223, https://doi.org/10.1021/ct200202g.
[46] G.S. Hammond, A correlation of reaction rates, J. Am. Chem. Soc. 77 (1955) 334–338, https://doi.org/10.1021/ja01607a027.
[47] R.A. Marcus, N. Sutin, Electron transfers in chemistry and biology, BBA Rev. Bioenerg. 811 (1985) 265–322, https://doi.org/10.1016/0304-4173(85)90014-X.
[48] R.a. Van Santen, M. Neurock, S.G. Shetty, Reactivity theory of transition-metal surfaces: a Bronsted–Evans–Polanyi linear activation energy: free-energy analysis, Chem. Rev. 110 (2010) 2005–2048. doi: 10.1021/cr9001808.
[49] J. Towns, T. Cockerill, M. Dahan, I. Foster, K. Gaither, A. Grimshaw, et al., XSEDE: accelerating scientific discovery, Comput. Sci. Eng. 16 (2014) 62–74, https://doi.org/10.1109/MCSE.2014.80.